JGR Oceans

RESEARCH ARTICLE
10.1029/2023JC020431

Modulation of Equatorial Currents and Tropical Instability Waves During the 2021 Atlantic Niño

Franz Philip Tuchen[1], Renellys C. Perez[1], Gregory R. Foltz[1], Peter Brandt[2,3], Ajit Subramaniam[4], Sang-Ki Lee[1], Rick Lumpkin[1], and Rebecca Hummels[2]

[1]NOAA/Atlantic Oceanographic and Meteorological Laboratory, Miami, FL, USA, [2]GEOMAR Helmholtz Centre for Ocean Research Kiel, Kiel, Germany, [3]Faculty of Mathematics and Natural Sciences, Kiel University, Kiel, Germany, [4]Lamont-Doherty Earth Observatory, Columbia University, Palisades, NY, USA

Key Points:

- The developing 2021 Atlantic Niño led to weaker equatorial surface currents and reduced vertical shear of upper-ocean horizontal velocity
- Strong reduction of the surface flow, eddy flux, and meridional temperature gradient in May caused extremely weak and delayed tropical instability wave (TIW) season
- Reduced meridional TIW advection contributed to sharpen the north equatorial Chl-*a* front resulting in modest intraseasonal Chl-*a* variability

Correspondence to:

F. P. Tuchen,
franz.philip.tuchen@noaa.gov

Citation:

Tuchen, F. P., Perez, R. C., Foltz, G. R., Brandt, P., Subramaniam, A., Lee, S.-K., et al. (2024). Modulation of equatorial currents and tropical instability waves during the 2021 Atlantic Niño. *Journal of Geophysical Research: Oceans*, *129*, e2023JC020431. https://doi.org/10.1029/2023JC020431

Received 15 SEP 2023
Accepted 16 NOV 2023

Abstract In the boreal summer of 2021, the equatorial Atlantic experienced the strongest warm event, that is, Atlantic Niño, since the beginning of satellite observations in the 1970s. Such events have far-reaching impacts on large-scale wind patterns and rainfall over the surrounding continents. Yet, developing a paradigm of how Atlantic Niño interacts with the upper-ocean currents and intraseasonal waves remains elusive. Here we show that the equatorial Kelvin wave associated with the onset of the 2021 Atlantic Niño modulated both the background flow and the eddy flux of the equatorial upper-ocean circulation, causing an extremely weak and delayed tropical instability wave (TIW) season. TIW-induced variations of sea surface temperature (SST), sea surface salinity, sea surface height, and eddy temperature advection were exceptionally weak during May to July, the climatological peak of TIW activity, but rebounded in August when higher than normal variability was observed. Moored velocity data at 23°W show that during the peak of the 2021 Atlantic Niño from June to August, the Equatorial Undercurrent was deeper and stronger than usual. An anomalously weak eddy momentum flux strongly suppressed barotropic energy conversion north of the equator from May to July, likely contributing to low TIW activity. Reduced baroclinic energy conversion also might have played a role, as the meridional gradient of SST was sharply reduced during the Atlantic Niño. Despite extremely weak TIW velocities, modest intraseasonal variability of chlorophyll-a (Chl-*a*) was observed during the Atlantic Niño, due to pronounced meridional Chl-*a* gradients that partly compensated for the weak TIWs.

Plain Language Summary Every few years the eastern equatorial Atlantic Ocean is significantly warmer than usual during boreal summer. Such warm events are referred to as Atlantic Niño events, and share similarities with El Niño events in the Pacific. In 2021, the strongest Atlantic Niño in at least four decades was observed in the equatorial Atlantic. This study is the first that investigates the complex interaction between Atlantic Niño, tropical Atlantic upper-ocean currents, and equatorial waves based on various observational data sets. We show that the developing 2021 Atlantic Niño weakened both the background flow and the variability of near-surface currents in May, which in turn largely reduced the strength of intraseasonal (20–50 days) waves that are usually generated by instability of the upper-ocean zonal currents. As a consequence, the cooling effect that these waves usually have north of the equator and the warming effect along the equator vanished from May to July 2021. Interestingly, variability of chlorophyll concentration was enhanced, suggesting that enhanced meridional chlorophyll gradients compensated for reduced wave activity.

1. Introduction

Variability of sea surface temperature (SST) in the tropical Atlantic is a powerful driver of climate variability over the surrounding continents (e.g., Folland et al., 2001; Foltz et al., 2019; Vallès-Casanova et al., 2020) and alters marine ecosystems through associated wind-induced upwelling of nutrients and resultant primary productivity (Grodsky et al., 2008; Radenac et al., 2020). On interannual time scales, tropical Atlantic SST variability is largely dominated by two seasonally phase-locked climate modes: the Atlantic meridional mode (AMM) and the Atlantic zonal mode (AZM). The positive and negative phases (i.e., warm and cold events) of the AZM are often referred to as Atlantic Niño and Niña events in reference to their Pacific counterparts, El Niño and La Niña (e.g., Lübbecke et al., 2018; Nobre & Shukla, 1996; Zebiak, 1993). While the AMM is defined as the anomalous meridional SST gradient between the northern and southern tropical Atlantic and is most pronounced from April to May (e.g., Chiang & Vimont, 2004; Foltz & McPhaden, 2010b; Rugg et al., 2016), the AZM is characterized by the timing, zonal extent, and intensity of a cold tongue of SST anomalies that forms in the central and

eastern Atlantic during boreal summer (e.g., Hormann et al., 2013; Zebiak, 1993). Atlantic Niños are extreme warm events that can cause severe rainfall and flooding over the Gulf of Guinea, West Africa, and northeastern South America (e.g., Lübbecke et al., 2018; Nobre & Shukla, 1996; Vallès-Casanova et al., 2020). They can impact other equatorial basins through atmospheric teleconnections (Ding et al., 2012; Losada et al., 2010; Rodríguez-Fonseca et al., 2009) and have been shown to intensify tropical cyclone development in the Cape Verde region (Kim et al., 2023). However, weather and climate models struggle to represent and predict Atlantic Niño and Niña events (Richter et al., 2017). This deficiency is often attributed to weaker coupling between the ocean and the atmosphere in the equatorial Atlantic Ocean compared to the Pacific Ocean (Richter et al., 2014), pointing toward the need for a better understanding of the physical processes involved.

Atlantic Niño events can be initiated in multiple ways (e.g., Lübbecke et al., 2018; Vallès-Casanova et al., 2020). In analogy to the Pacific Ocean, coupled air-sea Bjerknes feedback (Bjerknes, 1969) is generally viewed as the leading generation mechanism for Atlantic Niño and Niña events (Keenlyside & Latif, 2007): (a) zonal wind anomalies in the western basin are forced by SST anomalies in the eastern basin; (b) thermocline depth anomalies in the eastern basin are forced by zonal wind anomalies in the western basin; and (c) SST anomalies in the eastern basin are then forced by the thermocline depth anomalies. All three components of the Bjerknes feedback have been found to be active in the Atlantic (e.g., Deppenmeier et al., 2016; Keenlyside & Latif, 2007; Prigent et al., 2020). The second component of the Bjerknes feedback describes the adjustment of the equatorial thermocline slope to wind stress forcing at the surface: a low-baroclinic mode, downwelling (upwelling), equatorial Kelvin wave is excited by westerly (easterly) wind anomalies in the western equatorial Atlantic such that it flattens (steepens) the thermocline slope and increases (decreases) the upper-ocean heat content as it propagates eastward along the equator. However, some warm events occur in the absence of equatorial westerly wind anomalies and seem to be forced instead by off-equatorial North Atlantic anomalous westerly winds (Foltz & McPhaden, 2010a; Lübbecke & McPhaden, 2013). As suggested by Richter et al. (2013) such off-equatorial forced events might be excited by equatorward advection of temperature anomalies or through off-equatorial westward-propagating Rossby waves reflecting into eastward-propagating equatorial Kelvin waves at the western boundary. The strong 2021 Atlantic Niño, however, seems to have been driven by a combination of off-equatorial and equatorial wind and wave forcing (S.-K. Lee et al., 2023; Song et al., 2023). S.-K. Lee et al. (2023) showed that the Kelvin wave that initiated the 2021 Atlantic Niño was excited by an off-equatorial Rossby wave (see also Burmeister et al., 2016) that reflected as an equatorial Kelvin wave off the Brazilian coast and that was reinforced by westerly wind bursts (WWBs) in the central and western equatorial Atlantic Ocean. The WWBs were associated with enhanced convection of the Madden-Julian Oscillation over the Atlantic.

The influence of equatorial Kelvin waves on upper-ocean variability has been studied in models and observations for both the Pacific (Escobar-Franco et al., 2022; Holmes & Thomas, 2016) and the Atlantic Ocean (Hormann & Brandt, 2009). Hormann and Brandt (2009) showed that Kelvin wave activity during an Atlantic Niño event in 2002 exceeded Kelvin wave activity during an Atlantic Niña event in 2005, and that a strong downwelling Kelvin wave in 2002 caused a flatter east-west thermocline slope and a reduction in the core depth of the Equatorial Undercurrent (EUC) at 23°W. Using controlled numerical experiments, Holmes and Thomas (2016) focused on the interaction of Kelvin waves and tropical instability waves (TIWs) in model simulations of the Pacific Ocean. They found that downwelling Kelvin waves reduce the meridional shear of the zonal background flow and thereby reduce the kinetic energy of TIWs by 38%, while upwelling Kelvin waves have the opposite effect on TIWs and increase their kinetic energy by 42%. Weaker (stronger) TIW activity shortly after a downwelling (upwelling) Kelvin wave was also observed by Inoue et al. (2019) during the 2008/2009 Pacific TIW season. Although Holmes and Thomas (2016) examined the response of TIW kinetic energy to equatorial Kelvin waves, they did not specifically focus on the link between these events and developing El Niño or La Niña variations. More recently, Escobar-Franco et al. (2022) confirmed that TIW activity is decreased during the passage of downwelling Kelvin waves using 26 years of satellite altimetry data. They further pointed out the role of TIWs as a feedback mechanism on ENSO variability through meridional, nonlinear dynamic heating, that can cause asymmetric ENSO phases (see also Xue et al., 2023). However, to our knowledge, a detailed observational analysis of the response of equatorial currents and TIW activity to an Atlantic Niño event has not yet been conducted. A few previous studies point to an anticorrelation of AZM phases and TIW activity, but the empirical relationship is not statistically robust (Olivier et al., 2020; Perez et al., 2012; Wu & Bowman, 2007).

TIWs are the dominant source of intraseasonal (20–50 days) variability in the central equatorial Atlantic (Körner et al., 2022; Tuchen et al., 2018) and have been observed in sea surface temperature (Athié & Marin, 2008; Tuchen,

Perez, et al., 2022), sea surface salinity (T. Lee et al., 2014; Olivier et al., 2020; Tuchen, Perez, et al., 2022), sea surface height (Athié & Marin, 2008; von Schuckmann et al., 2008; Perez et al., 2012; Tuchen, Perez, et al., 2022), near-surface currents (Heukamp et al., 2022; Perez et al., 2019; Tuchen et al., 2018; Tuchen, Perez, et al., 2022), surface Chl-*a* concentration (Grodsky et al., 2008; Menkes et al., 2002; W. Shi & Wang, 2021), nutrients (Sherman et al., 2022), and oxygen (Eddebbar et al., 2021). TIWs are important components of the regional budgets of these variables, and year-to-year variations, low-frequency variability, and long-term trends of TIW activity may modulate the seasonal imprint of TIW-induced variability. In the Pacific Ocean, where TIW and Kelvin wave signals are easier to separate spatially and where warm/cold events are more pronounced than in the Atlantic Ocean, it is suggested that La Niña conditions favor stronger TIW activity and El Niño conditions favor weaker TIW activity (e.g., An, 2008; Wu & Bowman, 2007). TIWs can therefore act as an asymmetric negative feedback on ENSO with a cooling effect during El Niño and a ∼60% stronger warming effect during La Niña (An, 2008). In particular, the interaction of Niño/Niña events, TIWs, and surface chlorophyll-a concentration (Chl-*a*) variability poses a challenge for observational studies. Tian et al. (2019) showed that TIW-induced Chl-*a* variability modulates the penetration of shortwave radiation and feeds back onto ENSO variability: compared to an experimental run in which TIW-induced Chl-*a* variability is excluded, their control run produces an ENSO amplitude that is 27% larger. For the Atlantic Ocean, however, TIW-induced Chl-*a* variability is a largely overlooked research topic. Supported by the expanding coverage of ocean color data by overlapping satellite missions, Chl-*a* data availability has improved recently, allowing for a detailed analysis of Chl-*a* variability at TIW scales under the seasonal influence of Atlantic Niño conditions in 2021.

In light of recent findings of an observed weakening of tropical Atlantic SST variability (Prigent et al., 2020) and a projected weakening of Atlantic Niño variability (Crespo et al., 2022; Yang et al., 2022), it is important to investigate and quantify the impact that such extreme events have on the upper equatorial ocean. The aim of this study is a comprehensive analysis of the oceanic impacts of the exceptionally strong 2021 Atlantic Niño, with a focus on near-surface currents, Kelvin wave propagation, TIW activity, and surface Chl-*a* concentration.

2. Data

2.1. Satellite and Reanalysis Data

Estimates of wind stress are derived from ERA5 horizontal wind speed at 10 m provided on a 0.25° horizontal grid and at 1-hr intervals (Hersbach et al., 2020), which are here averaged to daily means. The horizontal wind speed components ($\vec{u_{10}}$) are converted to wind stress ($\vec{\tau}$) via a bulk formula: $\vec{\tau} = \rho_a c_D \vec{u_{10}} |\vec{u_{10}}|$, where ρ_a is the density of air (1.22 kg m^{-3}), and c_D the drag coefficient (assumed to be a constant value of 0.0013). Daily SST fields from the NOAA Optimally Interpolated SST data set (OI-SST version 2.1) are available since September 1981 on a 0.25° horizontal grid (Huang et al., 2021). Daily sea level anomaly (SLA) data are provided by the Copernicus Marine Environment Monitoring Service (CMEMS) since January 1993 with 0.25° horizontal resolution (version vDT2021). Version vDT2021 uses a two-satellite constellation in order to obtain homogeneous data coverage. We further use daily sea surface salinity (SSS) data which have been made available by the Soil Moisture Active Passive (SMAP) mission and are available since April 2015 on a 0.25° horizontal grid (Meissner et al., 2018). Several (partly overlapping) satellite missions have measured ocean color data since September 1997 and are used to infer surface Chl-*a* concentration. Since cloud coverage prevents satellite measurements in the visible light spectrum, data gaps are common in the tropical rain belt. To provide gap-free time series of surface Chl-*a* concentration, products have been developed that merge data from multiple sensors and use data-interpolating empirical orthogonal functions. Here, we use the Copernicus-GlobColour daily composites of surface Chl-*a* concentration at 4 km horizontal resolution provided since September 1997 (Copernicus, 2023b). The Copernicus product is constrained by in situ observations from numerous sources and databases (see "User Manual" and "Quality Information Document" under the provided reference for more details).

2.2. Moored Observations

In situ observations of current velocities and subsurface temperature are provided by moored surface buoys at 0°, 23°W and at 4°N, 23°W. Near-surface velocity measurements at 0°, 23°W are complemented by velocity data from a subsurface mooring in close proximity to the moored surface buoy (Tuchen, Brandt, et al., 2022). Data from the moored surface buoys and upper-ocean velocity data from the subsurface mooring are part of the

Prediction and Research Moored Array in the Tropical Atlantic (PIRATA; Bourlès et al., 2019; Foltz et al., 2019). The moored surface buoys are equipped with an acoustic current meter at a depth of around 10 m and have provided real-time velocity data since the years 2005 and 2006 at 0° and 4°N, respectively, while the subsurface mooring on the equator covers the upper ocean with an upward-looking Acoustic Doppler Current Profiler (ADCP) located at around 220 m since 2001 with few gaps at the beginning of the time series (Tuchen, Brandt, et al., 2022). Due to the reflection of the acoustic signal at the ocean surface, ADCP measurements near the surface are corrupted and the shallowest data point from the subsurface mooring is usually at 20 m depth. Velocity data from both the moored surface buoy and the subsurface mooring on the equator are combined into one comprehensive data set that is publicly available (Tuchen, Brandt, et al., 2022). Here we use the most recent version (v2.0) covering measurements from December 2001 to June 2023 (Tuchen et al., 2023).

2.3. Drifter-Wind-Altimetry Synthesis

Global, daily maps of near-surface current velocities are made available from a synthesis of drifter measurements, wind-derived Ekman velocities, and geostrophic velocities from satellite altimetry (Lumpkin & Garzoli, 2011). The most recent version of this data set covers the time period from 1993 to 2021 and is provided on a 0.25° horizontal grid. Although it has been shown that this product tends to underestimate the observed high-frequency velocity fluctuations on the equator (Tuchen, Perez, et al., 2022), it is a valuable data source for examining the zonal background flow in the tropical and equatorial Atlantic during the 2021 Atlantic Niño. This data product is used to investigate TIW activity north of the equator, where TIW-induced SLA variability is strongest (e.g., Athié & Marin, 2008; Perez et al., 2012) and a pronounced band of barotropic energy conversion is observed, that is, conversion of mean kinetic energy into eddy kinetic energy (von Schuckmann et al., 2008; Tuchen, Perez, et al., 2022).

3. Results

3.1. Overview of the 2021 Atlantic Niño Event

The 2021 Atlantic Niño was generated by a combination of WWBs in the western and central equatorial Atlantic during the first week of May (Figure 1a) and a series of downwelling Rossby waves that were excited between January and April north of the equator. The Rossby waves propagated to the western boundary where they reflected into the Atlantic basin as downwelling equatorial Kelvin waves and were reinforced by the WWBs in the western and central equatorial Atlantic (cf. S.-K. Lee et al., 2023 for more details). The eastward propagation of positive SLA anomalies (Figure 1b) agrees well with the theoretical phase speed of a second baroclinic mode Kelvin wave, 1.4 m s^{-1} (Hormann & Brandt, 2009), and indicates a deepening thermocline. Shortly after the Kelvin wave crossed the Atlantic basin, sustained SST anomalies of more than +1°C developed in the central and eastern equatorial Atlantic (Figure 1c), with SST anomalies exceeding +2°C close to 10°W in June and July. The warm event lasted throughout boreal summer, with a slight disruption in September during the passing of an upwelling Kelvin wave, and plateaued at around 1°C from mid-September until the end of November (Figure 1c). The short-lived, weaker cooling signal observed in September was in good agreement with the theoretical eastward phase propagation speed of a first baroclinic mode Kelvin wave, 2.4 m s^{-1}. However, this upwelling Kelvin wave did not have a strong impact on the thermocline slope, thus causing only a brief weakening of the positive SST anomalies. It should be noted that although the observed phase speed will be close to the propagation speed of the dominant wave, the observed wave is really a superposition of freely propagating equatorial Kelvin waves and locally forced waves.

Pronounced negative anomalies in Chl-*a* of up to −0.2 mg m^{-3} were observed during the 2021 Atlantic Niño from June to August (Figure 1d) that are seemingly anticorrelated with the positive SST anomalies and the deeper thermocline. However, in contrast to sustained positive SST anomalies, negative Chl-*a* anomalies did not persist beyond August and largely relaxed back to climatological values during boreal fall. The Atlantic Niño and its positive SST anomalies decayed in December, making it one of the longest-lived warm events on record. The decay of SST anomalies coincides with a pronounced upwelling Kelvin wave (i.e., second baroclinic mode) propagating from the western boundary in late December to the eastern boundary in late January with phase speed near 1.4 m s^{-1}. While SST anomalies relaxed during boreal winter and the thermocline shoaled, a pronounced Chl-*a* bloom developed (Figure 1d), excited by the passage of the upwelling Kelvin wave and in good

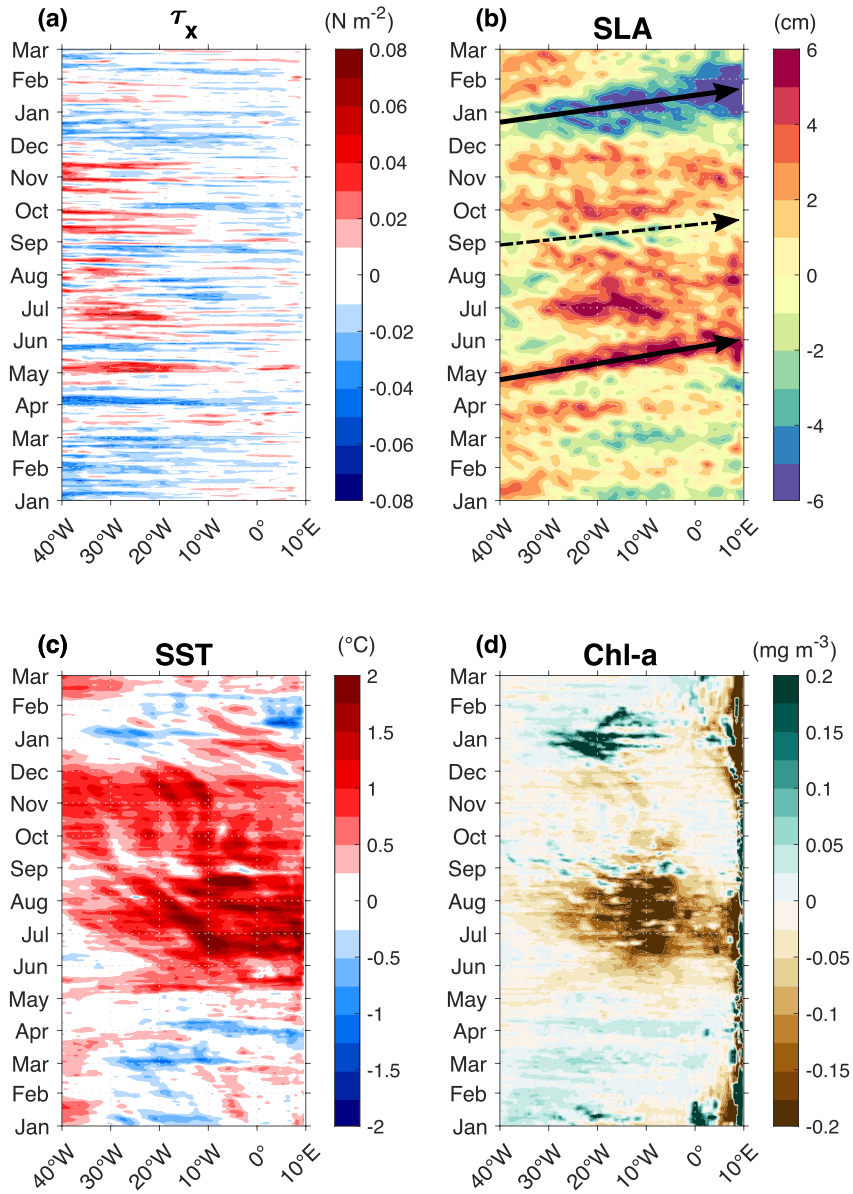

Figure 1. January 2021 to March 2022 equatorial anomalies of (a) zonal wind stress (τ_x), (b) sea level anomaly (SLA), (c) sea surface temperature (SST), and (d) surface chlorophyll-a concentration (Chl-*a*). All variables have been averaged between 1°N and 1°S and filtered with a 3 days and 0.75° longitude moving average. All anomalies are calculated with respect to the daily climatological value at each grid point computed from the complete length of the individual time series. The solid arrows in (b) indicate the theoretical propagation speed of a second baroclinic mode equatorial Kelvin wave (1.4 m s^{-1}). The dash-dotted arrow in (b) indicates the theoretical propagation speed of a first baroclinic mode Kelvin wave (2.4 m s^{-1}).

agreement with negative SST anomalies. Although it is well known that Chl-*a* shows a pronounced semiannual cycle with peaks in boreal summer and winter (Brandt et al., 2023; Grodsky et al., 2008), the 2021–2022 wintertime bloom greatly exceeded climatological values, making it the strongest wintertime Chl-*a* bloom on record (see Section 3.4).

3.2. Impact of the 2021 Atlantic Niño on Equatorial Currents

We first examine the response of near-surface ocean currents to the 2021 Atlantic Niño as observed in the drifter-wind-altimetry synthesis product and mooring data. The mean surface zonal flow (*u*) in the equatorial Atlantic is characterized by the northern and the central branches of the westward South Equatorial Current

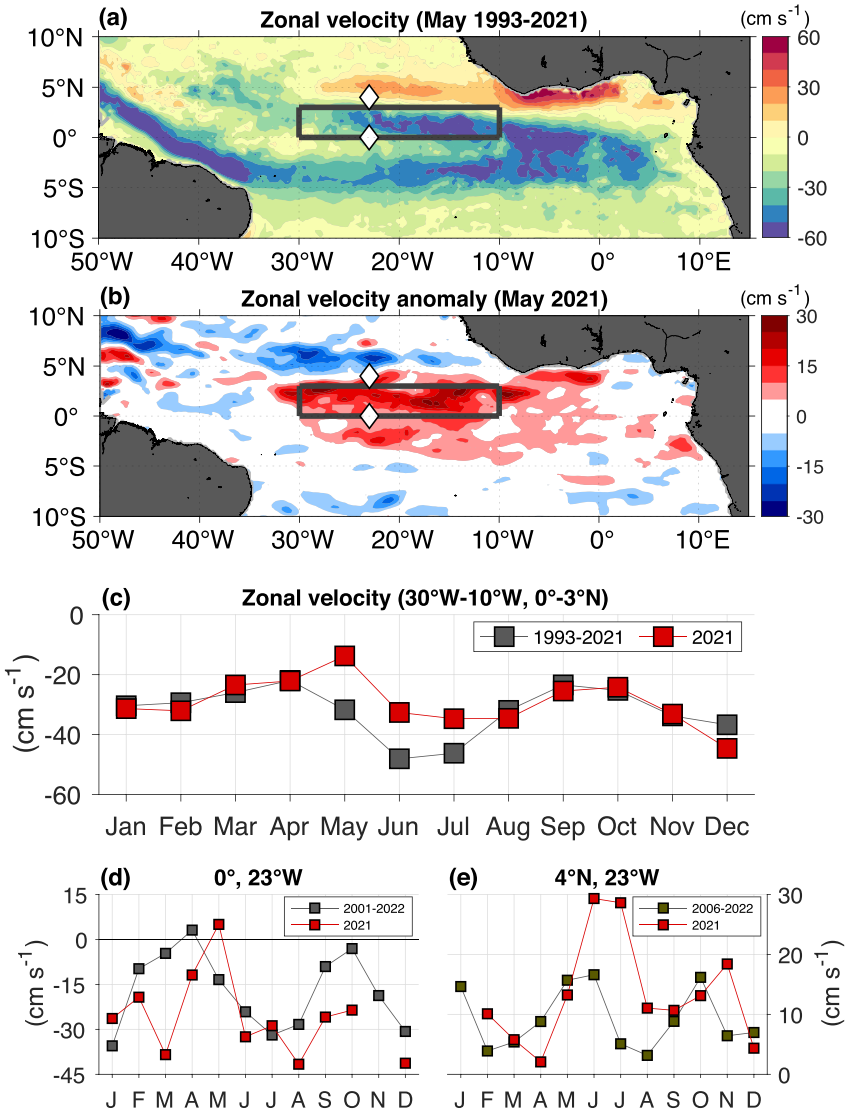

Figure 2. (a) Monthly mean near-surface zonal velocity derived from the drifter-wind-altimetry synthesis during May computed from 1993 to 2021, (b) zonal velocity anomaly in May 2021, (c) monthly mean zonal velocity within the nSEC region indicated by box (30°W–10°W, 0°–3°N) in (a) and (b) from 1993 to 2021 (gray squares) and for 2021 (red squares). The white diamonds in (a, b) indicate the moored buoy locations at 0°, 23°W and 4°N, 23°W for which the long-term means (gray squares) and the 2021 monthly values of zonal velocity are shown in (d, e), respectively.

(nSEC and cSEC) centered at around 1–2°N and 3–4°S, respectively, and the eastward North Equatorial Countercurrent (NECC) centered at around 5°N (Figure 2a). In particular, the region between the NECC and the nSEC exhibits strong meridional shear of zonal velocity generating a pronounced band of barotropic energy conversion (e.g., von Schuckmann et al., 2008; Specht et al., 2021). During the onset of the Atlantic Niño in May 2021, when the initial downwelling Kelvin wave propagates along the equatorial Atlantic, the westward flow between 4°N and 4°S is greatly weakened (Figure 2b). Most notably, the westward nSEC is reduced by about 15 cm s^{-1} (averaged between 30°W–10°W, 0°–3°N) compared to its climatological value of about −30 cm s^{-1} and remains weaker than usual during June and July (Figure 2c). Near-surface velocity data from the equatorial moored surface buoy at 23°W confirms the reduction of westward flow in May (Figure 2d); its eastward anomalies are of the same magnitude as those from the drifter-wind-altimetry synthesis product for the region centered around the nSEC. At 4°N, 23°W, eastward velocities are close to climatological values in May, but the anomalous eastward flow increases from 10 cm s^{-1} in June to 20 cm s^{-1} in July (Figure 2e). The latitudinal range in which equatorial Kelvin waves impact upper-ocean variability depends partly on the vertical mode of the wave, but the wave

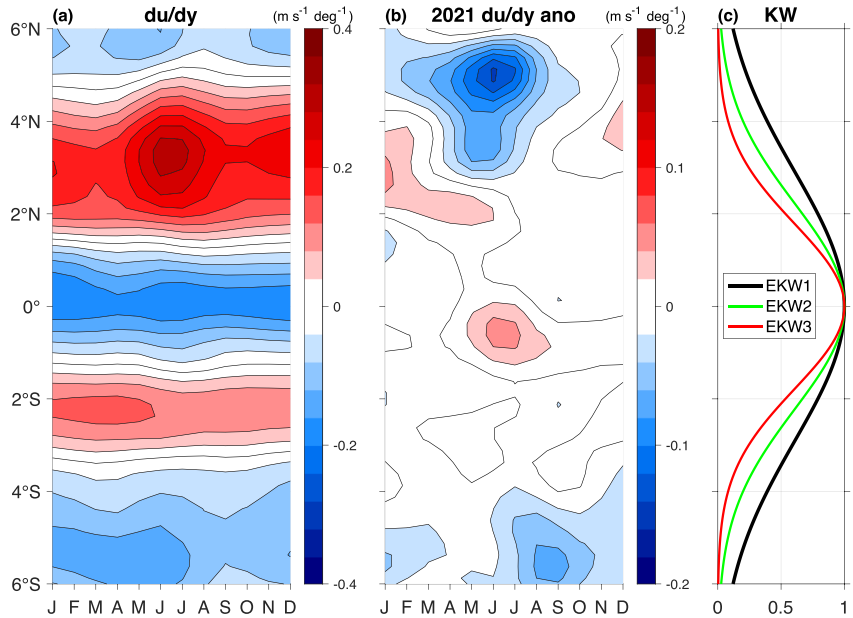

Figure 3. (a) Climatological meridional gradient of zonal velocity (*du/dy*) averaged between 30°W and 10°W, (b) anomalous *du/dy* for 2021 averaged between 30°W and 10°W from the drifter-wind-altimetry synthesis product. Monthly anomalies are given with respect to the long-term mean (1993–2021). (c) Theoretical meridional structure of the first (black), second (green), and third (red) baroclinic mode equatorial Kelvin wave (EKW) reconstructed from $\eta(y) = \eta_0 \exp\left(-\beta y^2/2c\right)$ with $\eta_0 = 1$, $\beta = df/dy = 2.28 * 10^{-11}$ m^{-1} s^{-1}, f Coriolis parameter, y distance from the equator, and $c = 2.4$ m s^{-1} (1.4 m s^{-1}, 0.9 m s^{-1}) the phase velocity of a first (second, third) baroclinic mode equatorial Kelvin wave at 23°W (Hormann & Brandt, 2009).

amplitude declines exponentially away from the equator. Hence, at 4°N, the meridional influence of a second vertical mode Kelvin wave is largely reduced.

Holmes and Thomas (2016) suggested that a downwelling Kelvin wave reduces the meridional shear between the nSEC/NECC and between the nSEC/EUC, causing an overall reduction in TIW kinetic energy. In contrast to their numerical findings, our results show that during the 2021 Atlantic Niño, which was initiated by a strong downwelling Kelvin wave, there is relatively little impact on the meridional shear of zonal velocity (*du/dy*) near the equator (Figure 3). Near the surface, monthly climatological values of *du/dy* are characterized by alternating positive and negative values between the NECC, nSEC, equatorial flow minimum, and the cSEC (Figure 3a). As positive *du/dy* is required to provide energy to TIWs via barotropic energy conversion, the presence of negative *du/dy* anomalies would be consistent with weaker TIWs. Monthly *du/dy* anomalies are virtually zero between 4°S and 3°N, except near the equator in June and July when weak positive *du/dy* anomalies are observed in a region with typically negative *du/dy* and near 2°N from February to June where weak positive *du/dy* anomalies are observed that would reinforce the positive climatological values (Figure 3b). However, larger negative anomalies are observed near 3°N from May to June and from 4°N to 6°N from March to July, reducing the typically positive *du/dy* at this latitude and consistent with weaker TIWs. As mentioned above, the meridional structure of a second vertical mode Kelvin wave indicates a reduced influence on latitudes beyond 4° latitude (Figure 3c). By mainly suppressing westward flow near the equator, the Kelvin wave is expected to reduce positive shear between the NECC and nSEC which is only partly observed (Figure 3b). Therefore, the changes in zonal flow close to the equator are likely caused by a superposition of the eastward-propagating Kelvin wave and the Rossby wave response (Perez & Kessler, 2009) to local wind forcing and stratification (background temperature and salinity gradients) and cannot be explained by the passage of the Kelvin wave alone. However, the drifter-wind-altimetry synthesis product only provides a near-surface view. Next, we turn to moored velocity observations on the equator at 23°W for a subsurface perspective.

Zonal velocity (u) in the central equatorial Atlantic is mainly characterized by variability on semiannual and annual time scales (Brandt et al., 2016). In the upper 200 m, u is dominated by the EUC and its seasonal intensification and vertical migration (Brandt et al., 2014). The core depth of the EUC is typically located between 50 and 90 m, but during early and mid-2021 the EUC core was persistently 5–10 m deeper than usual (Figure 4a). The deepening

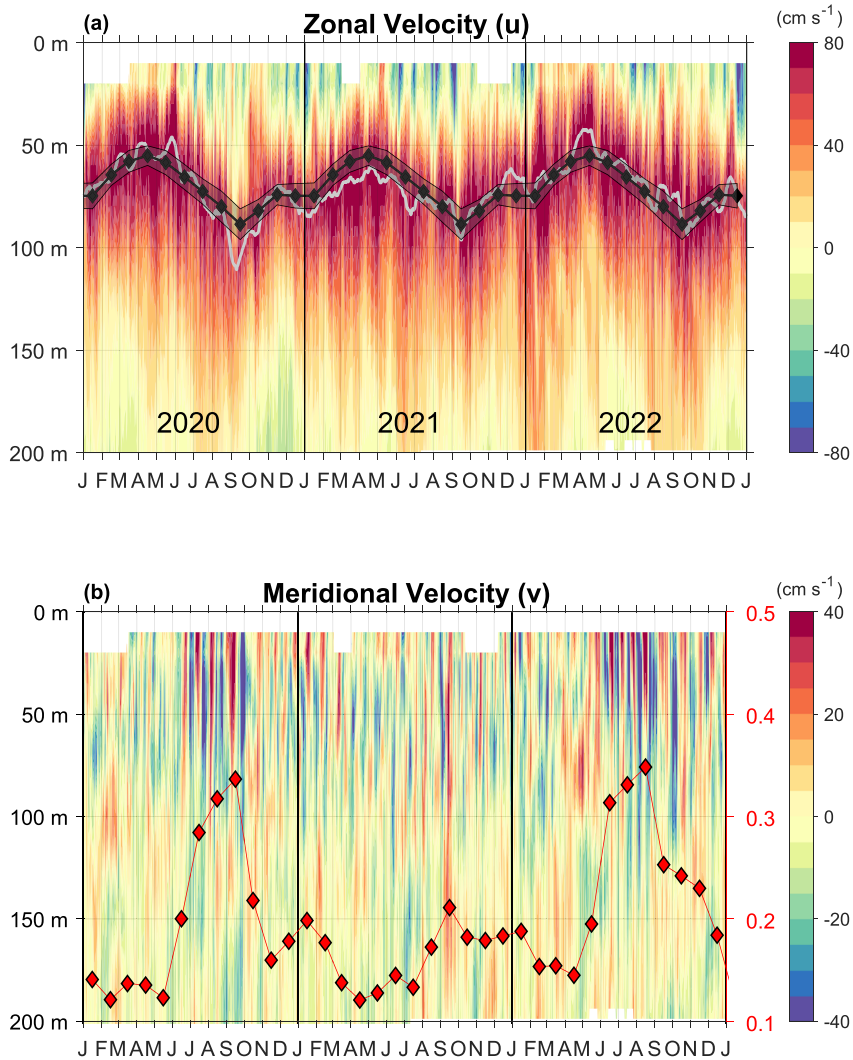

Figure 4. Upper-ocean (a) zonal velocity, and (b) meridional velocity as observed at the moored observatory at 0°, 23°W between 2020 and 2022. The gray line in (a) marks the maximum zonal velocity for each time step as an indicator of the Equatorial Undercurrent (EUC) core depth, while the black diamonds show the monthly climatological EUC core depth with the standard error envelope (dark gray shading). The red diamonds in (b) represent the tropical instability wave (TIW) index, that is, the monthly standard deviation of intraseasonal meridional velocity defined between the surface and 50 m depth (in m s^{-1}). Note the active TIW seasons in 2020 and 2022 in comparison to weak activity in 2021.

of the EUC roughly coincides with more westward velocities close to the surface in the first half of 2021, except for a short burst of eastward velocity anomalies reaching from the EUC core to the surface in May 2021, which is associated with the passage of the equatorial Kelvin wave at the mooring site. Interestingly, the EUC is deeper than usual during its usually shallowest phase in April/May, suggesting that the fourth baroclinic mode that dominates the annual cycle of zonal velocity and that has a zero-crossing near the EUC core depth (Brandt et al., 2016) is likely modified during the onset of the Atlantic Niño. Prior to an Atlantic Niño event in 2002, Hormann and Brandt (2009) observed a flattening of the thermocline slope and a shallower EUC core at 23°W. This is in contrast to our findings which show a consistently deeper than usual EUC core in the boreal summer of 2021. Meridional velocity (v) fluctuations are dominated by intraseasonal variability due to the propagation of TIWs primarily during boreal summer, but TIWs are sometimes present in fall and winter (Figure 4b). Moored velocity observations show that intraseasonal meridional velocity fluctuations (red diamonds in Figure 4b) were strikingly reduced in the boreal summer of 2021, and weak summertime TIW activity is observed.

To further disentangle the impacts of the 2021 Atlantic Niño on subsurface velocities, we examine the monthly mean vertical profiles of anomalous u (Figure 5a), eddy kinetic energy (EKE; Figure 5b), vertical gradient of zonal

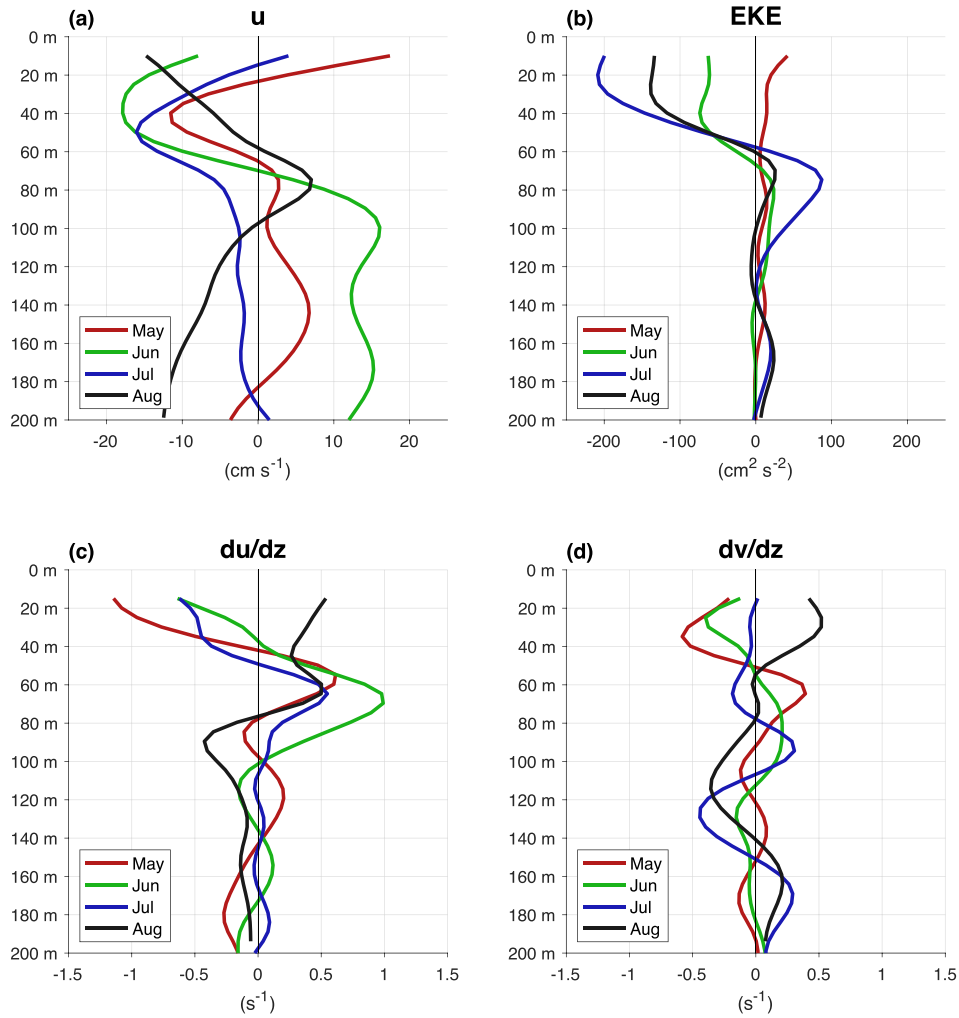

Figure 5. Vertical profiles of monthly mean anomalies of (a) zonal velocity (*u*), (b) eddy kinetic energy (EKE), (c) vertical shear of zonal velocity (*du*/*dz*), and (d) vertical shear of meridional velocity (*dv*/*dz*) from May to August 2021 from moored velocity data at 0°, 23°W.

velocity (*du*/*dz*; Figure 5c), and vertical gradient of meridional velocity (*dv*/*dz*; Figure 5d) during May-August 2021 as observed at 0°, 23°W. In agreement with our previous results, near-surface (upper 20 m) eastward anomalies during May were as large as 15 cm s^{-1}, while at about 40 m, westward anomalies of more than −10 cm s^{-1} were observed (red line in Figure 5a). This is in agreement with a deeper than usual EUC enabling near-surface westward velocities to reach larger depths and shifting the maximum vertical shear of zonal velocity to larger depths (red line in Figure 5c). This vertical shift becomes most apparent during June (green line in Figure 5a), with westward velocity anomalies of close to −20 cm s^{-1} at 40 m and a deeper EUC at 23°W causing eastward anomalies of more than 10 cm s^{-1} from about 80 to 200 m. Westward flow anomalies at around 40–60 m prevail in July (blue line in Figure 5a), but this pattern clearly changes in August (black line in Figure 5a). Particularly important is the reduced *du*/*dz* above the EUC from May to July (Figure 5c), which is likely associated with the deeper than normal EUC and also possibly the weaker westward flow close to the surface. As the westward near-surface flow is associated with the nSEC at 1°N, strongly reduced horizontal shear between the EUC and the nSEC is expected. However, because the drifter-wind-altimetry synthesis product only provides velocities at an estimated depth of 15 m, the horizontal shear at EUC depth cannot be assessed. It is noteworthy that positive anomalies of *du*/*dz* are observed in the upper 40 m in August (black line in Figure 5c), indicating a dynamical shift that is also observed in *dv*/*dz* close to the surface (Figure 5d) where negative anomalies are present from May to July and positive anomalies are observed in August. EKE near the surface is greatly reduced from June to August, consistent with reduced TIW activity after the passage of the Kelvin wave in May (Figure 5b).

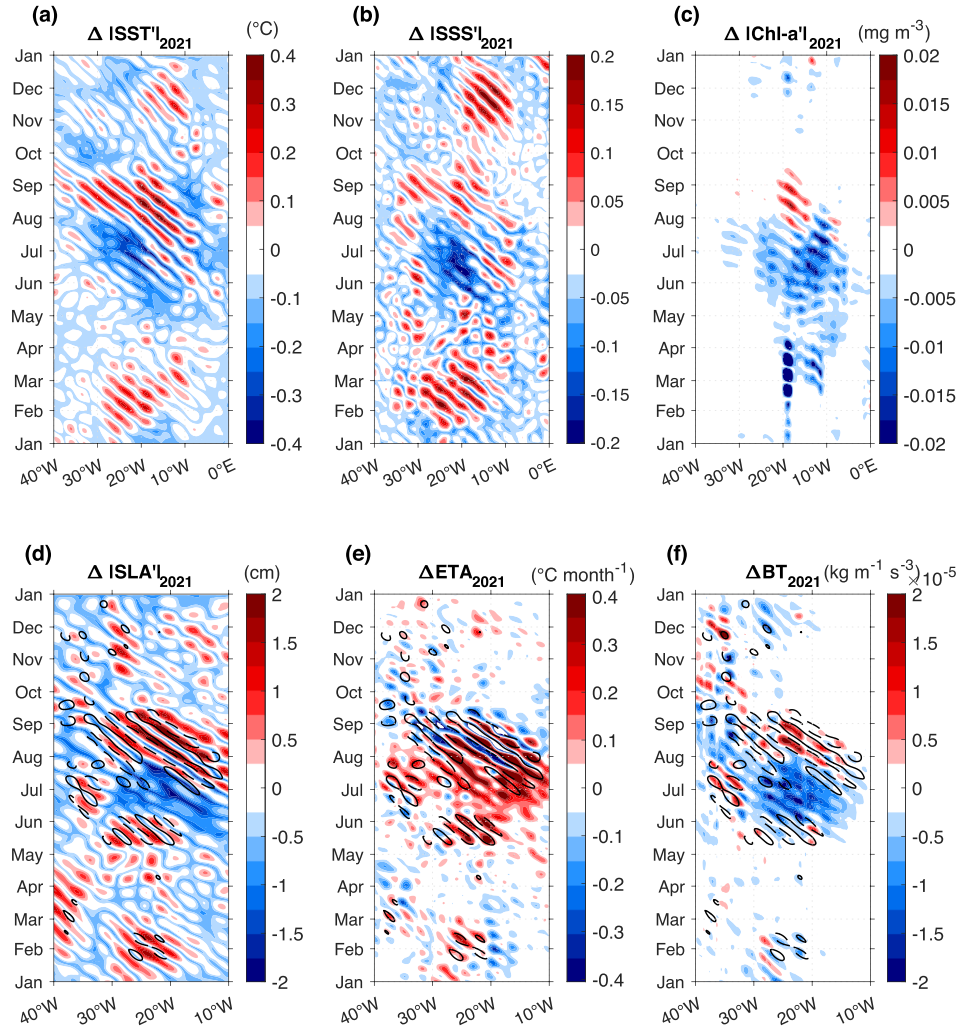

Figure 6. Hovmoeller diagrams of anomalous 2021 tropical instability wave (TIW) activity for (a) sea surface temperature (SST) at 1°N, (b) sea surface salinity (SSS) at 1°N, (c) surface chlorophyll-a concentration (Chl-*a*) at 1°N, (d) sea level anomaly (SLA) at 4°N, and anomalous (e) eddy temperature advection (ETA) at 4°N, and (f) barotropic energy conversion (BT) at 4°N. The difference (Δ) from the daily climatological seasonal cycle at each grid point is shown. Note that for (a–d) the difference of the absolute intraseasonal anomalies (e.g., |SST′|) is used in order to preserve negative and positive phases of the individual waves, whereas in (e, f) differences are computed of the intraseasonal anomalies themselves. The contour lines in (d–f) show the 7 cm s^{-1} band-pass filtered near-surface meridional velocity (dashed: negative, solid: positive) from the drifter-wind-altimetry synthesis.

3.3. The Extremely Weak 2021 Tropical Instability Wave Season

Recent findings suggest that TIW activity was strongly reduced during the boreal summer of 2021 compared with the summertime TIWs of the last three to four decades (Tuchen, Perez, et al., 2022). One goal of this study is to quantify how the 2021 Atlantic Niño impacted TIW activity and to investigate potential mechanisms. To isolate variability due to TIWs, the time series have been temporally (20–50 days) and zonally (4°–20° longitudes) band-pass filtered with a second-order Hamming window. Variables to which this filter is applied are indicated by a prime (e.g., u'). In a first step, we focus on the anomalous 2021 TIW season as observed in SST, SSS, Chl-*a* (all at 1°N where these parameters usually show highest TIW-induced variability, e.g., Tuchen, Perez, et al., 2022; Figures 6a–6c), and SLA at 4°N (Figure 6d). The Hovmoeller diagrams of anomalous TIW-induced variability show a clear reduction for all parameters during May-July when compared to climatological values. Interestingly, TIW-induced variability is not uniformly reduced throughout the entire summer of 2021, but rebounds in August when higher than normal variability is observed for the four parameters. This results in a delayed onset of the 2021 TIW season and suppression of TIW activity during the climatological peak months of these parameters:

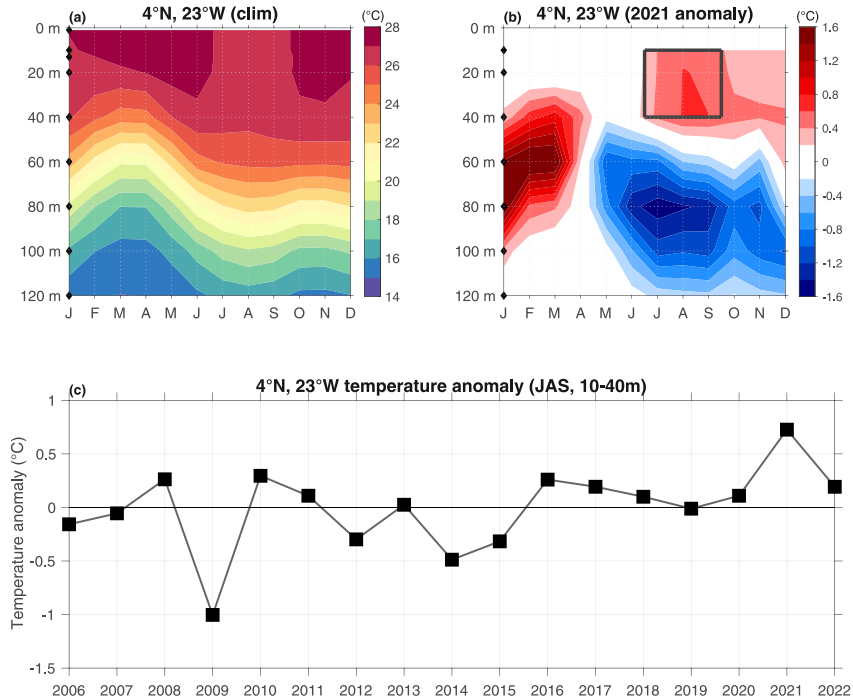

Figure 7. (a) Climatological seasonal cycle of subsurface temperature (0–120 m) at the 4°N, 23°W PIRATA moored surface buoy between 2006 and 2022. (b) Anomalous seasonal cycle of subsurface temperature at 4°N, 23°W in 2021. Black diamonds in (a, b) indicate depths at which moored temperature sensors are available. (c) Upper-ocean (10–40 m) temperature anomaly during July to September at 4°N, 23°W as indicated by the black box in (b).

July for the peak of TIW-induced variability in SST and Chl-*a* at 1°N, and SLA at 4°N, and June for the peak of TIW-induced SSS variability at 1°N (e.g., Olivier et al., 2020; Tuchen, Perez, et al., 2022).

Using near-surface velocities provided by the drifter-wind-altimetry synthesis, we investigate the eddy temperature advection (ETA) at 4°N due to TIWs ($-(u'dT'/dx + v'dT'/dy)$, Figure 6e). At 4°N, the TIW-induced ETA, which is usually negative and provides an advective cooling effect, is largely reduced from May to July 2021. In fact, positive ETA anomalies (Figure 6e) are so strong that the advective cooling effect is reversed, leading to advective warming from May to June (not shown). A decomposition of the upper-ocean temperature anomalies at 4°N into individual contributions from TIW activity, surface heat fluxes, and others is complicated by the limited available observations. Nevertheless, analyzing subsurface temperatures from the moored surface buoy at 4°N, 23°W shows a strong warming signal from June to September 2021 (Figure 7b) that could be due in part to the extremely weak TIW season (i.e., warming due to the reduction of TIW-induced advective cooling). In fact, positive temperature anomalies of about 0.7°C (averaged between July to September and from 10 to 40 m) are unprecedented when considering the available time series at this mooring site covering the years 2006–2022 (Figure 7c). Although not shown, meteorological observations available at the mooring demonstrate that incoming shortwave radiation was weaker than usual at 4°N, 23°W in 2021 (i.e., negative anomalies, tending to cool SST), but latent heat flux shows positive anomalies (warming) from January–June 2021 of comparable magnitude with anomalous temperature advection (warming) due to TIWs. This suggests that suppressed TIW activity combined with anomalous latent heat flux played a substantial role in driving positive SST anomalies north of the equator.

As one generation mechanism for TIWs, the anomalous barotropic energy conversion ($BT = -\rho_0 \overline{u'v'} d\overline{U}/dy$) along 4°N is evaluated next (Figure 6f). BT was largely reduced from May to July (negative anomalies in Figure 6f), in agreement with overall weak TIW activity during those months, while in August stronger than usual BT (positive anomalies) is observed. TIWs are primarily generated by baroclinic and barotropic instability, which convert potential energy into EKE and mean kinetic energy into EKE, respectively. Near-surface BT can be estimated fairly well from velocity data provided by the drifter-wind-altimetry synthesis off the equator, while observational estimates of equatorial BT have higher uncertainty due to underestimated intraseasonal flow variability in gridded data products (Tuchen, Perez, et al., 2022). North of the equator BT usually peaks from June to

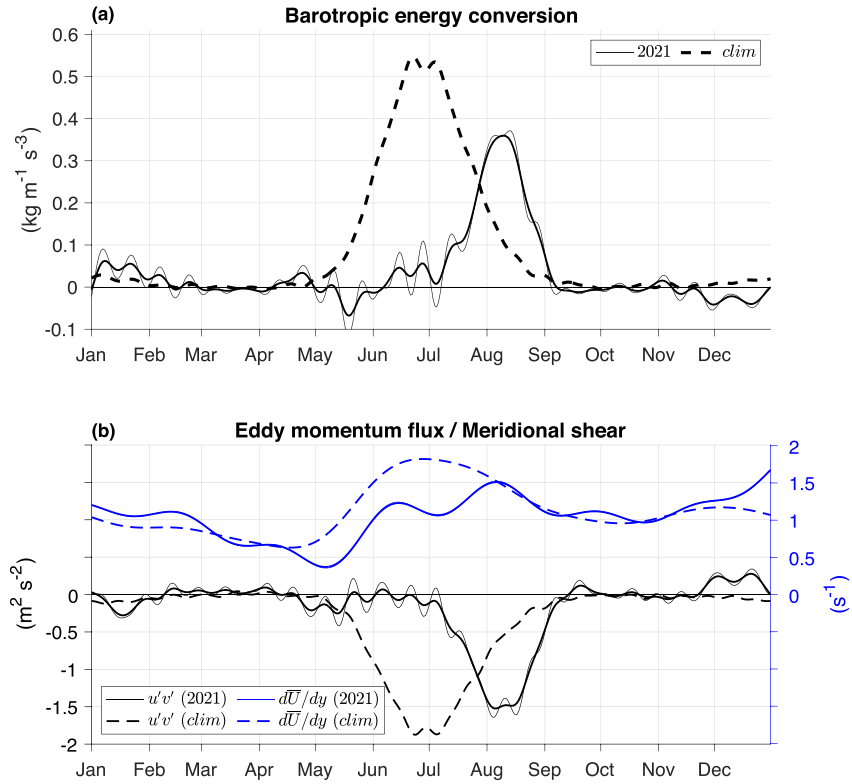

Figure 8. (a) Barotropic energy conversion ($\times 10^{-5}$) between 2°N–6°N, 30°W–10°W in 2021 (solid lines; thin: daily, thick: 15 days running mean applied) and climatology (dashed), (b) individual components of the barotropic energy conversion term in 2021: eddy momentum flux ($u'v'$; black; $\times 10^{-5}$), and meridional shear of zonal background flow ($d\overline{U}/dy$; blue; $\times 10^{-3}$). $\overline{U}$ is defined as the 50-day low-pass filtered zonal velocity using a second-order Hamming window.

July when both components, the eddy momentum flux ($\overline{u'v'}$) and the meridional shear of background zonal flow ($d\overline{U}/dy$; where $\overline{U}$ is the 50-day low-pass filtered zonal flow using a second-order Hamming window), peak as well (dashed lines in Figure 8). Clearly, the 2021 seasonal intensification of BT is delayed by 2 months (solid line in Figure 8a). Although the amplitude of the seasonal BT maximum in August 2021 is weaker than the climatological BT maximum in June-July, it is about 3 times stronger than the typical BT amplitudes observed in August (Figure 8a). When separating BT into its components, Figure 8b shows that the shear term is slightly weaker than normal during June and July 2021 (compare blue lines), and there is an obvious 2-month delay in the peak of the eddy momentum flux in 2021 relative to climatology (compare black lines), which leads to the 2-month delay in the overall BT maximum. The amplitude of eddy momentum flux in August 2021 is comparable to the amplitude of the climatological peak that occurs during June-July. Hence, we conclude that a temporal shift in the eddy momentum flux predominantly caused the delay in TIW activity in 2021, while the reduced meridional shear provided background conditions favorable for suppressed TIW activity.

Baroclinic energy conversion cannot be estimated directly because of unavailable vertical velocity observations, but it is tightly linked to horizontal density gradients in the vicinity of the equatorial cold tongue (e.g., Yu et al., 1995). Thus, horizontal density gradients, which are largely controlled by meridional SST gradients at the surface, can be used as a proxy for baroclinic energy conversion. First, we examine the meridional SST gradient (dSST/dy) in the equatorial Atlantic, which is governed by the seasonal evolution of the cold tongue in boreal summer, when dSST/dy is maximum north of the equator (Figure 9a). Note that because meridional SST gradients are stronger than zonal gradients (dSST/dx), we only consider the meridional component here. At 1°N, where the strongest meridional gradient is typically observed, dSST/dy is positive year-round. The 2021 season reveals a strong reduction of dSST/dy centered on May-July north of the equator, consistent with the arrival of the initial Kelvin wave in May and the subsequent warming of the equatorial Atlantic, which prevents the full development of the cold tongue (Figure 9b). Weak meridional SST gradients are suggested to have three impacts. First, they reduce the TIW-induced SST variability by smoothing the typically sharp SST front north of the

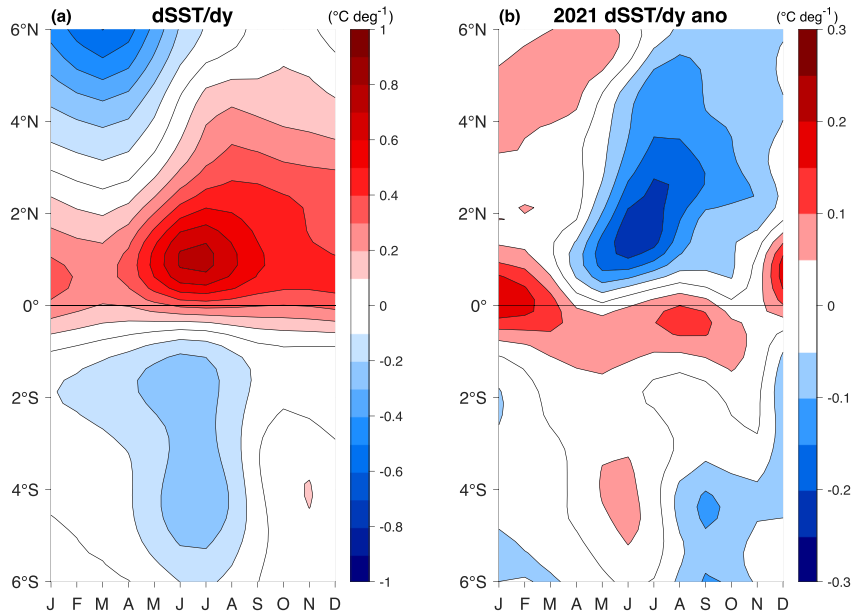

Figure 9. (a) Climatological meridional gradient of SST (*d*SST/*dy*) averaged between 30°–10°W, (b) anomalous *d*SST/*dy* for 2021 averaged between 30°–10°W. Monthly anomalies are given with respect to the long-term mean (1982–2022).

equator where TIWs usually cause the highest SST variability (Perez et al., 2012). Second, through the gradient wind balance, weak *d*SST/*dy* reduces the meridional gradient of zonal geostrophic velocity, which counteracts the wind-driven Ekman shear near the equator (not shown) and contributes to the observed weak *du*/*dy* anomalies in 2021 (Figure 3b). Third, baroclinic instability as a generation mechanism for TIWs is likely reduced by a weak north equatorial SST front. The persistence and the magnitude of the reduction in *d*SST/*dy* over a time period of 3–4 months is unprecedented in the >40-year SST record. Similarly, the pronounced increase of *d*SST/*dy* later in December 2021 and January 2022 is a record-breaking positive anomaly and likely contributed to the development of strong wintertime TIW activity through enhanced baroclinic energy conversion. Note, we find no striking signal in the horizontal gradients of sea surface salinity (SSS) anomalies (not shown), and for that reason did not use *d*SSS/*dy* as an indicator of anomalous baroclinic energy conversion.

3.4. Intraseasonal Variability of Surface Chlorophyll-a Concentration

In this section, we will quantify how TIW-induced Chl-*a* variability responded to the exceptional 2021 Atlantic Niño. Chl-*a* in the central equatorial Atlantic (20°W-0°, 3°S–3°N; the ATL3 region) was at its lowest summertime level in June and July 2021 since the start of satellite-based ocean color measurements in 1997 (not shown). Another outstanding feature of the Chl-*a* time series in the central equatorial Atlantic (Figure 10a) is a pronounced wintertime bloom from December 2021 to January 2022 that is unprecedented in the whole record. Besides year-to-year fluctuations of the seasonal summer and winter maxima, pronounced intraseasonal fluctuations between June to August are observed for all years at varying amplitudes (0.1–0.3 mg m^{-3}). The periodicity and seasonality of these intraseasonal fluctuations in the central equatorial Atlantic is indicative of TIWs.

However, as described above, TIW velocities were extremely weak during the summer of 2021 (Figure 4b). One possible explanation for the modest Chl-*a* variability of about 0.1 mg m^{-3} in 2021, despite weak TIW velocities, is that pronounced horizontal gradients of Chl-*a* compensated for weak TIW velocities. In general, summertime amplitudes of meridional Chl-*a* gradients (*d*Chl-*a*/*dy*, Figure 10b) reach 0.1–0.2 mg m^{-3} deg^{-1} and are about 2–4 times larger than zonal Chl-*a* gradients (*d*Chl-*a*/*dx*, Figure 10c), as expected from seasonal upwelling that is typically strongest along the equator in the summer and generates sharp fronts to the north and south (see Figure 11a). *d*Chl-*a*/*dy* values in summer 2021 were at levels comparable to those in 2020 and 2022, especially in August, when both zonal and meridional Chl-*a* gradients have elevated amplitudes of about 0.09 and 0.03 mg m^{-3} deg^{-1}, respectively. Interestingly, the winter Chl-*a* peak in 2021–2022 is characterized by an extremely pronounced *d*Chl-*a*/*dy* peak (~0.2 mg m^{-3} deg^{-1}; Figure 10b) that is the largest *d*Chl-*a*/*dy* winter peak in the past 20 years

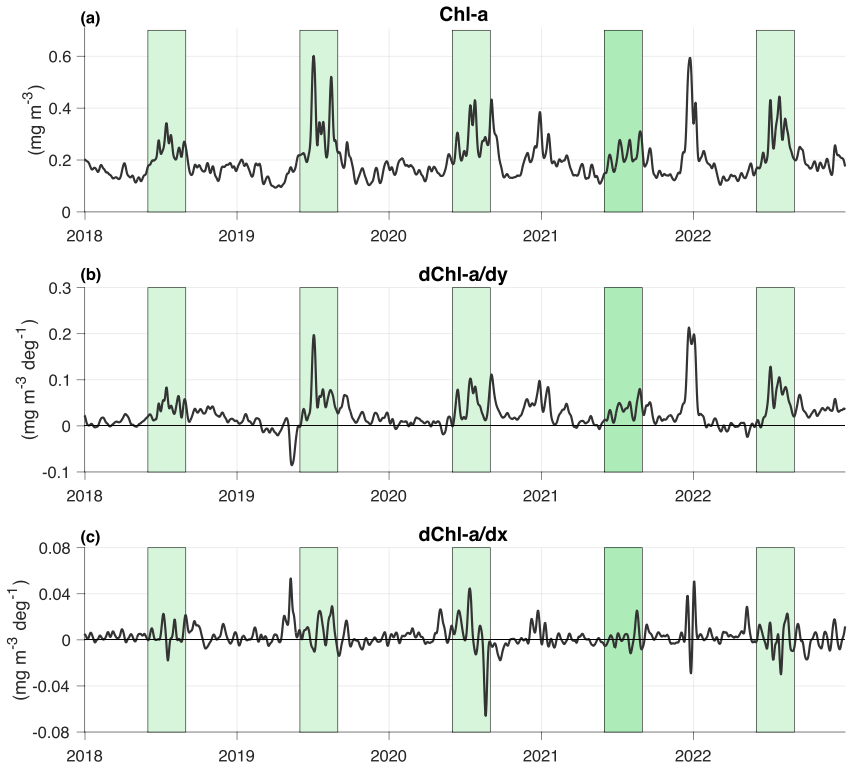

Figure 10. Time series of (a) surface chlorophyll-a concentration (Chl-*a*), (b) meridional Chl-*a* gradient (*d*Chl-*a*/*dy*), and (c) zonal Chl-*a* gradient (*d*Chl-*a*/*dx*) at 0°–2°N, 25°W–21°W. The yearly June-July-August time periods are marked in green. A 15-day running mean is applied to all time series.

and is only exceeded by the *d*Chl-*a*/*dy* peak in summer 2014 (not shown). Overall, *d*Chl-*a*/*dx* is less correlated with TIW seasonality (Figure 10c), but may occasionally contribute to sharper horizontal Chl-*a* fronts during times when *d*Chl-*a*/*dy* is weak.

In contrast to the equatorial cold tongue with its asymmetric SST fronts north and south of the equator (Figure 9a), the climatological Chl-*a* fronts are more symmetric with opposite signs about the equator (Figure 11a). In summer 2021, the near-equatorial Chl-*a* fronts north and south of the equator were weaker than normal, with the south equatorial gradient more reduced than the north equatorial gradient (Figure 11b). At 1°N, where TIW-induced variability of Chl-*a* is most pronounced on average, *d*Chl-*a*/*dy* was relatively close to climatological values in summer 2021 (Figure 11c). Hence, we conclude that horizontal Chl-*a* gradients, especially in the meridional direction, likely contributed to keeping TIW-induced Chl-*a* variability at a relatively high level, despite extremely weak TIW velocities.

Another measure of the relative role of horizontal Chl-*a* gradients in driving TIW-induced Chl-*a* variability is the eddy advection term, which can be calculated analogously to eddy temperature advection: $-\left(u' d\text{Chl-}a'/dx + v' d\text{Chl-}a'/dy\right)$. Zonal and meridional eddy Chl-*a* advection (ECA) were estimated at the 0°, 23°W and 4°N, 23°W mooring sites (Figure 12). Estimates with near-surface velocities from the drifter-wind-altimetry synthesis largely underestimate ECA both on the equator and to a lesser degree at 4°N, 23°W, where estimates are more similar to ECA from moored velocities (not shown). Here, negative values indicate an advective loss of Chl-*a* due to eddies, that is, TIWs in this context, while positive values indicate an advective gain of Chl-*a*. The north equatorial region at 4°N, 23°W is typically associated with an advective gain of Chl-*a* from April to July (zonal; Figure 12a) and from May to August (meridional; Figure 12b) due to summertime TIW activity. In contrast, on the equator TIWs act to decrease Chl-*a* from July to December (zonal; Figure 12c) and from May to July (meridional; Figure 12d). In 2021, this pattern was reversed at 4°N, 23°W, where advective loss of Chl-*a* is observed throughout the year for the meridional component and is most pronounced in August. On the equator, meridional ECA is reduced from May to July, meaning that less than usual Chl-*a* is advected away from the equator, possibly causing an accumulation of upwelled Chl-*a* on the

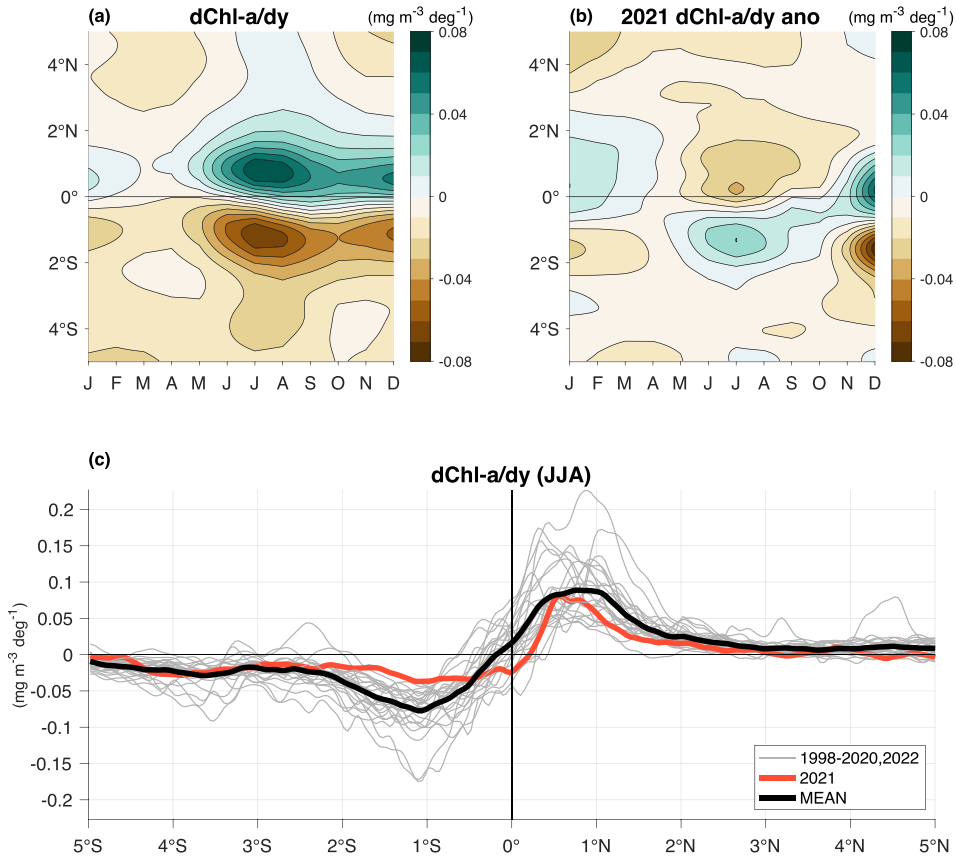

Figure 11. (a) Climatological meridional gradient of surface chlorophyll-a concentration (*d*Chl-*a*/*dy*) averaged between 25°W–21°W, (b) anomalous *d*Chl-*a*/*dy* for 2021 averaged between 25°W–21°W. Monthly anomalies are given with respect to the 1998–2022 mean. (c) Boreal summer (June-August) mean *d*Chl-*a*/*dy* between 25°W–21°W as a function of latitude for each year (colors), and long-term climatological mean (black; MEAN).

equator. Little change is observed in zonal ECA at the equator compared to other years (Figure 12c). Similar to TIW-induced variability of physical parameters (see Figure 6), stronger than usual meridional ECA is observed in August. As a consequence, during boreal summer of 2021 less Chl-*a* is advected away from the equator and the equatorial Chl-*a* front is sustained rather than being reduced due to TIW activity. The resultant sharp Chl-*a* gradients might have enhanced TIW-induced Chl-*a* variability and could be a pathway through which modest TIW-induced Chl-*a* variability can result from relatively weak TIW velocities earlier in the season.

4. Discussion

The presented results provide an assessment of the impacts of the 2021 Atlantic Niño on the upper equatorial ocean, with a focus on the modulation of equatorial currents and seasonal TIW activity in both physical and biogeochemical parameters. The downwelling equatorial Kelvin wave that initiated the Atlantic Niño caused a strong reduction of near-surface westward flow close to the equator during May 2021. This is in agreement with a recent study by Martín-Rey et al. (2023), who found that the nSEC is weakened during the onset of an Atlantic Niño event. However, while they showed that subsurface currents change little, we observe strengthening and deepening of the Equatorial Undercurrent (EUC) during the onset of the Atlantic Niño from May to June. Our findings also contrast with those of Góes and Wainer (2003) and Hormann and Brandt (2009) who found that the EUC core was shallower and weaker during warm events and deeper and stronger during cold events. While an overall weakening of the EUC during an Atlantic Niño is an intuitive response to reduced easterlies at the surface, our findings point out that this relation might be reversed during the onset of an extreme warm event. Such an acceleration and deepening of the EUC was observed during the 1983 Atlantic Niño event (Hisard & Hénin, 1987).

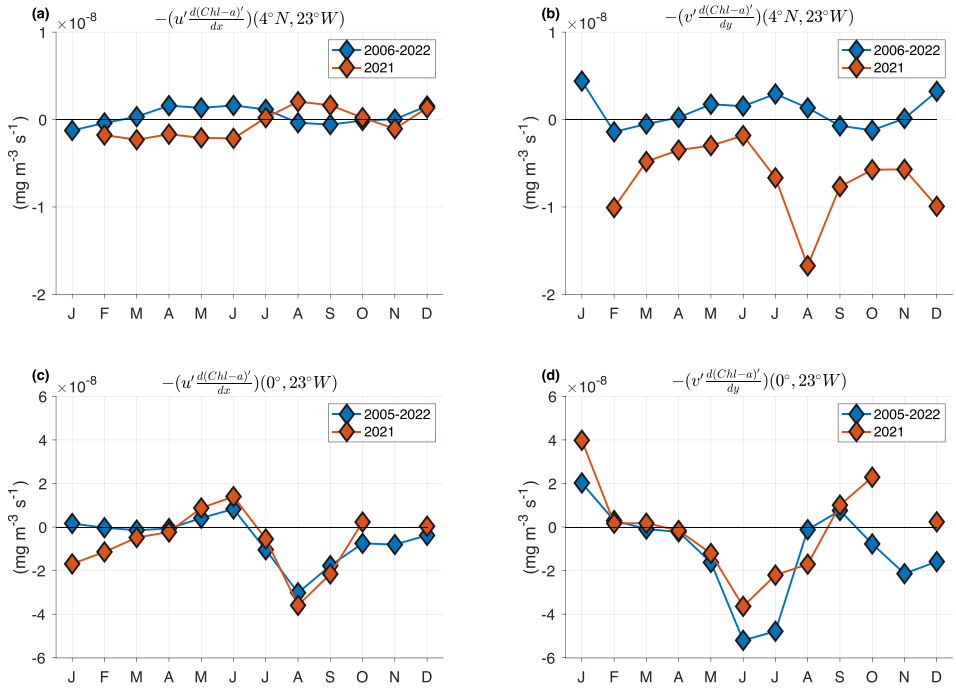

Figure 12. Monthly averages of (a) zonal ($(-(u'dChl - a'/dx))$) and (b) meridional ($(-(v'dChl - a'/dy))$) eddy Chl-*a* advection at 4°N, 23°W derived from moored velocity observations from 2006 to 2022 (blue diamonds) and during 2021 (red diamonds). Monthly averages of (c) zonal and (d) meridional eddy Chl-*a* advection at 0°, 23°W derived from moored velocity observations from 2005 to 2022 (blue diamonds) and during 2021 (red diamonds). Both horizontal velocity and surface Chl-*a* concentration have been band-pass filtered (20–50 days). Negative values indicate an advective loss of Chl-*a*, while positive values indicate an advective gain of Chl-*a*.

The rapid weakening of westward flow near the surface in response to the passage of the strong, downwelling Kelvin wave had less impact on the meridional shear of zonal velocity near the equator in the drifter-wind-altimetry synthesis than expected. It should be noted, however, that there is higher uncertainty in the drifter-wind-altimetry synthesis horizontal velocity estimates close to the equator (Tuchen, Perez, et al., 2022). In fact, near-surface moored velocity data at 0°, 23°W do show stronger than normal westward flow before and after the Kelvin wave pulse (Figures 2d and 5a), and the 4°N, 23°W mooring observed a strong eastward anomaly, indicative of increased meridional shear. However, it is possible that the strongest eastward velocity anomaly occurred between 0° and 4°N and was largely unnoticed by in situ observations at subsurface level. According to the model study by Holmes and Thomas (2016), downwelling Kelvin waves considerably reduce the meridional shear of the zonal currents and therefore result in lower levels of TIW kinetic energy. The cause of the discrepancy is likely the broad and spatially uniform weakening of the surface zonal flow between 4°N and 4°S during the passage of the Kelvin wave, which when combined with local wind and density gradients did not introduce significant meridional shear anomalies except for some weakened shear between 2°N and 6°N. This demonstrates that in order to represent the nuanced temporal and vertical evolution of the subsurface circulation during an Atlantic Niño, high temporal resolution (monthly or shorter time scales) velocity observations are needed.

Despite only weak changes in the meridional shear of zonal velocity, a pronounced reduction of TIW activity was observed in SST, SSS, SLA, and meridional velocity, and to some extent also Chl-*a*, as is typically expected during an El Niño event (An, 2008). Such a strong and uniform TIW response to the 2021 Atlantic Niño, across multiple parameters, is unprecedented. At 4°N, 23°W the extremely low TIW activity caused a reversal of the eddy temperature advection (i.e., advective heating instead of advective cooling due to TIWs) which coincided with positive latent heat flux anomalies. These two factors contributed to the highest summertime upper-ocean temperatures north of the equator in at least 15 years. However, colocated observations of atmospheric and oceanic parameters, which are needed to calculate heat fluxes and heat budget, are only available at a few distinct sites in the equatorial Atlantic. This motivates future process studies to investigate the temporal-spatial structure of heat flux anomalies during extreme events like the 2021 Atlantic Niño. One promising approach is the use of

uncrewed surface vehicles and underwater gliders in combination with enhanced coverage of floats and surface drifting buoys.

To further understand the reason for the extremely weak 2021 TIW season and the rebound of TIW activity in August, we examined the barotropic energy conversion term, that is, the product of meridional shear of zonal velocity and eddy momentum flux. The absence of barotropic energy conversion north of the equator during June and July 2021, when the term is usually at its maximum (Tuchen, Perez, et al., 2022), was followed by a late peak in August that was mainly driven by a similarly delayed peak in the eddy momentum flux. An obvious, but not easy to answer, question is: what drove the delay in the eddy momentum flux in the first place? Moored observations on the equator show that the vertical shear of both zonal velocity and meridional velocity close to the surface was reduced during May to July, which is indicative of reduced horizontal shear between the EUC and nSEC. Similarly, increased vertical shear of horizontal velocity in August, when the EUC is shallower than normal, might have forced increased barotropic and baroclinic instability. Vertical displacement and adjustment of surface and subsurface zonal currents in response to equatorial waves during the 2021 Atlantic Niño is one possible explanation for the exceptional intraseasonal anomalies of eddy momentum flux during the summer of 2021.

Another focus of this study was to quantify the modulation of TIW-induced Chl-*a* variability in response to the 2021 Atlantic Niño. First of all, it is noteworthy that the boreal summer Chl-*a* concentrations in 2021 were the lowest in more than a decade, while the boreal winter Chl-*a* concentrations in late 2021—early 2022 were the highest since the start of satellite observations in 1997. From model experiments in the Pacific Ocean, it has been shown that TIW-induced Chl-*a* variability causes a 27% increase in ENSO amplitude compared to a model run with no TIW-induced Chl-*a* variability (Tian et al., 2019). Recently, it was shown that the surface Chl-*a* feedback effect on ENSO amplitude is similar to that of interannual variations of the deep Chl-*a* maximum (Q. Shi et al., 2023). Dedicated numerical model experiments or focused observational campaigns are required to further examine TIW-induced Chl-*a* variability at the surface and, in particular, in the subsurface and its feedback on Atlantic Niño amplitude in more detail. In our analysis, we find pronounced intraseasonal variations of surface Chl-*a* even with strongly reduced TIW velocities. However, to generate Chl-*a* variability, TIWs must either exhibit pronounced velocities or act on sharp horizontal Chl-*a* gradients. In fact, horizontal Chl-*a* gradients in the summer of 2021 are of comparable amplitude as in other years, especially at 1°N, where typically the highest TIW-induced Chl-*a* variability is observed. Evans et al. (2009) found that weak TIWs maintain nutrient levels and increase Chl-*a* concentrations due to suppressed advective processes. Here, we hypothesize that weak TIW velocities sustain the sharpness of the equatorial Chl-*a* front due to reduced eddy advection, that is, less advective loss of Chl-*a* due to TIWs. However, a more conclusive relation between TIWs and Chl-*a* variability is complicated by several unknown factors, such as local production, decay, vertical distribution and upwelling of Chl-*a*.

5. Conclusions

The 2021 Atlantic Niño caused exceptionally strong, positive SST anomalies over the whole equatorial Atlantic Ocean from June to December. This extreme warm event was the strongest since the start of satellite measurements in the 1970s and therefore provided a unique opportunity to study its impacts on the upper equatorial ocean in great detail. In this study we focused on the modulation of equatorial currents and tropical instability wave (TIW) activity during the 2021 Atlantic Niño. The main new insights are:

- During the passage of the strong, downwelling Kelvin wave that initiated the 2021 Atlantic Niño, a strong, brief, reduction of the westward near-surface currents was observed. In contrast to previous findings, a smaller than expected change in the meridional shear of zonal velocity was observed close to the equator suggesting that local (wind and buoyancy) processes must have compensated for the effect of the Kelvin wave. In the subsurface, a stronger and deeper than normal EUC was present during the onset of the 2021 Atlantic Niño.
- TIW-induced variability in SST, SSS, SLA, and meridional velocity was sharply reduced from May to July, when those parameters usually peak climatologically. Elevated TIW activity in August, after the climatological TIW peak, indicates that the 2021 TIW season was not only weaker than usual, but also delayed. Barotropic energy conversion was also delayed, with a peak in August driven primarily by a temporal shift in the eddy momentum flux. The north equatorial meridional SST gradient was largely reduced from May to July, suppressing both TIW-induced SST variability and baroclinic energy conversion. This is the first time

that such a strong and multiparameter weakening of TIW activity has been observed in response to a strong Atlantic Niño.

- Despite weak TIW velocities, near-normal levels of intraseasonal Chl-*a* variability were observed probably because meridional Chl-*a* gradients partly compensated for the weak meridional velocities. In fact, weak TIW velocities are hypothesized to sustain a sharp Chl-*a* front because of weaker eddy advection that normally reduces Chl-*a* and its meridional gradient north of the equator. More research is required to disentangle the impact of TIWs on Chl-*a* variability from other processes such as local growth and decay.

Our results highlight the spatial and temporal complexity of the ocean's response to extreme events and the need to further advance our understanding of tropical Atlantic variability and its interactions with the upper ocean. The combination of extremely low Chl-*a* in boreal summer and the extreme high values the following winter are unprecedented in the last 25 years and deserve further attention as there could be impacts for marine ecosystems. A strong rebound of Chl-*a* after El Niño has been shown by both observations and model simulations for the Pacific Ocean (e.g., Chavez et al., 1999; Lim et al., 2022), where it provides a source of resilience for local marine ecosystems. Such a likely connection between Atlantic Niño and marine ecosystems will be an important motivation for future research.

Data Availability Statements

All data used in this analysis are publicly available. Satellite observations and reanalysis data used in this study are available at the following links: NOAA OI-SST version 2.1 (Huang et al., 2021), CMEMS-C3S-SLA version DT2021 (Copernicus, 2023c), Copernicus Global Ocean Colour (Copernicus GlobColour), Bio-Geo-Chemical L4 daily data (Copernicus, 2023b), JPL SMAP Level 3 Sea Surface Salinity data V5.0 (JPL, 2020), ECMWF ERA5 hourly 10-m horizontal wind speed (Copernicus, 2023a). The near-surface drifter-wind-altimetry synthesis data can be accessed via: https://www.aoml.noaa.gov/ftp/pub/phod/lumpkin/decomp/. Oceanic and atmospheric data obtained by moored surface buoys are made available through the PIRATA program (https://www.pmel.noaa.gov/tao/drupal/disdel/). Moored velocity observations at 0°, 23°W are provided through the World Data Center PANGAEA (Tuchen et al., 2023).

Acknowledgments
The authors thank Fabian Gomez, Kandaga Pujiana, and two anonymous reviewers for helpful comments and suggestions on the manuscript. This research was performed while FPT held a National Research Council (NRC) Research Associateship Award at NOAA's Atlantic Oceanographic and Meteorological Laboratory (AOML). RCP and GRF were supported by NOAA's Global Ocean Monitoring and Observing Program (funding reference number 100007298), under the PIRATA Northeast Extension project, and by AOML. PB and RH were supported by EU H2020 under Grant Agreement 817578 TRIATLAS project and by the Deutsche Forschungsgemeinschaft through several research cruises with R/V Meteor, R/V Maria S. Merian, and R/V Sonne. AS was supported by NASA Grant 80NSSC21K0439, funding from the G. Unger Vetlesen Foundation and a fellowship from Columbia University's Center for Climate and Life. SKL was supported by NOAA's Climate Program Office's Modeling, Analysis, Predictions, and Projections program. FPT, RCP, GRF, SKL, and RL acknowledge support by NOAA's AOML. RL was also supported by NOAA/GOMO Global Drifter Program funding. The authors thank the captains, crews, scientists, and technical groups involved in numerous research cruises to the tropical Atlantic that contributed to collecting shipboard and moored velocity data and making them freely available. Moored velocity observations were acquired by GEOMAR in cooperation with the PIRATA program supported by NOAA (USA), IRD and Meteo-France (France), INPE and the Brazil Navy (Brazil).

References

An, S.-I. (2008). Interannual variations of tropical ocean instability wave and ENSO. *Journal of Climate*, *21*(15), 3680–3686. https://doi.org/10.1175/2008JCLI1701.1

Athié, G., & Marin, F. (2008). Cross-equatorial structure and temporal modulation of intraseasonal variability at the surface in the tropical Atlantic Ocean. *Journal of Geophysical Research*, *113*, C08020. https://doi.org/10.1029/2007JC004332

Bjerknes, J. (1969). Atmospheric teleconnections from the equatorial Pacific. *Monthly Weather Review*, *97*(3), 163–172. https://doi.org/10.1175/1520-0493(1969)097<0163:ATFTEP>2.3.CO;2

Bourlès, B., Araujo, M., McPhaden, M. J., Brandt, P., Foltz, G. R., Lumpkin, R., et al. (2019). Pirata: A sustained observing system for tropical Atlantic climate research and forecasting. *Earth and Space Science*, *6*(4), 577–616. https://doi.org/10.1029/2018EA000428

Brandt, P., Alory, G., Awo, F. M., Dengler, M., Djakouré, S., Imbol Koungue, R. A., et al. (2023). Physical processes and biological productivity in the upwelling regions of the tropical Atlantic. *Ocean Science*, *19*(3), 581–601. https://doi.org/10.5194/os-19-581-2023

Brandt, P., Claus, M., Greatbatch, R. J., Kopte, R., Toole, J. M., Johns, W. E., & Böning, C. W. (2016). Annual and semiannual cycle of equatorial Atlantic circulation associated with basin-mode resonance. *Journal of Physical Oceanography*, *46*(10), 3011–3029. https://doi.org/10.1175/JPO-D-15-0248.1

Brandt, P., Funk, A., Tantet, A., Johns, W. E., & Fischer, J. (2014). The Equatorial Undercurrent in the central Atlantic and its relation to tropical Atlantic variability. *Climate Dynamics*, *43*(11), 2985–2997. https://doi.org/10.1007/s00382-014-2061-4

Burmeister, K., Brandt, P., & Lübbecke, J. F. (2016). Revisiting the cause of the eastern equatorial Atlantic cold event in 2009. *Journal of Geophysical Research: Oceans*, *121*, 4056–4076. https://doi.org/10.1002/2016JC011719

Chavez, F. P., Strutton, P. G., Friederich, G. E., Feely, R. A., Feldman, G. C., Foley, D. G., & McPhaden, M. J. (1999). Biological and chemical response of the equatorial Pacific Ocean to the 1997–98 El Niño. *Science*, *286*(5447), 2126–2131. https://doi.org/10.1126/science.286.5447.2126

Chiang, J. C. H., & Vimont, D. J. (2004). Analogous Pacific and Atlantic meridional modes of tropical atmosphere-ocean variability. *Journal of Climate*, *34*(21), 4143–4158. https://doi.org/10.1175/JCLI4953.1

Copernicus. (2023a). ERA5 hourly data on single levels from 1940 to present [Dataset]. Copernicus Climate Change Service (C3S), Climate Data Store (CDS). https://doi.org/10.24381/cds.adbb2d47

Copernicus. (2023b). Global Ocean Colour (Copernicus-GlobColour), Bio-Geo-Chemical, L4 (monthly and interpolated) from satellite observations (1997-ongoing) [Dataset]. Copernicus. https://doi.org/10.48670/moi-00281

Copernicus. (2023c). Sea level gridded data from satellite observations for the global ocean from 1993 to present [Dataset]. Copernicus Climate Change Service (C3S), Climate Data Store (CDS). https://doi.org/10.24381/cds.4c328c78

Crespo, L., Prigent, A., Keenlyside, N., Koseki, S., Svendsen, L., Richter, I., & Sánchez-Gómez, E. (2022). Weakening of the Atlantic Niño variability under global warming. *Nature Climate Change*, *12*(9), 822–827. https://doi.org/10.1038/s41558-022-01453-y

Deppenmeier, A. L., Haarsma, R. J., & Hazeleger, W. (2016). The Bjerknes feedback in the tropical Atlantic in CMIP5 models. *Climate Dynamics*, *47*(7–8), 2691–2707. https://doi.org/10.1007/s00382-016-2992-z

Ding, H., Keenlyside, N. S., & Latif, M. (2012). Impact of the equatorial Atlantic on the El niño southern Oscillation. *Climate Dynamics*, *38*(9–10), 1965–1972. https://doi.org/10.1007/s00382-011-1097-y

Eddebbar, Y. A., Subramanian, A. C., Whitt, D. B., Long, M. C., Verdy, A., Mazloff, M. R., & Merrifield, M. A. (2021). Seasonal modulation of dissolved oxygen in the equatorial Pacific by tropical instability vortices. *Journal of Geophysical Research: Oceans*, *126*, e2021JC017567. https://doi.org/10.1029/2021JC017567

Escobar-Franco, M. G., Boucharel, J., & DeWitte, B. (2022). On the relationship between tropical instability waves and intraseasonal equatorial Kelvin waves in the Pacific from satellite observations (1993–2018). *Frontiers in Marine Science*, *9*, 788908. https://doi.org/10.3389/fmars.2022.788908

Evans, W., Strutton, P. G., & Chavez, F. P. (2009). Impact of tropical instability waves on nutrient and chlorophyll distributions in the equatorial Pacific. *Deep-Sea Research I*, *56*(2), 178–188. https://doi.org/10.1016/j.dsr.2008.08.008

Folland, C. K., Colman, A. W., Rowell, D. P., & Davey, M. K. (2001). Predictability of Northeast Brazil rainfall and real-time forecast skill, 1987-98. *Journal of Climate*, *14*(9), 1937–1958. https://doi.org/10.1175/1520-0442(2001)014<1937:PONBRA>2.0.CO;2

Foltz, G. R., Brandt, P., Richter, I., Rodríguez-Fonseca, B., Hernandez, F., Dengler, M., et al. (2019). The tropical Atlantic observing system. *Frontiers in Marine Science*, *6*, 206. https://doi.org/10.3389/fmars.2019.00206

Foltz, G. R., & McPhaden, M. J. (2010a). Abrupt equatorial wave-induced cooling of the Atlantic cold tongue in 2009. *Geophysical Research Letters*, *37*, L24605. https://doi.org/10.1029/2010GL045522

Foltz, G. R., & McPhaden, M. J. (2010b). Interaction between the Atlantic meridional and Niño modes. *Geophysical Research Letters*, *37*, L18604. https://doi.org/10.1029/2010GL044001

Góes, M., & Wainer, I. (2003). Equatorial currents transport changes for extreme warm and cold events in the Atlantic Ocean. *Geophysical Research Letters*, *30*(5), 8006. https://doi.org/10.1029/2002GL015707

Grodsky, S. A., Carton, J. A., & McClain, C. R. (2008). Variability of upwelling and chlorophyll in the equatorial Atlantic. *Geophysical Research Letters*, *35*, L03610. https://doi.org/10.1029/2007GL032466

Hersbach, H., Bell, B., Berrisford, P., Hirahara, S., Horányi, A., Muñoz-Sabater, J., et al. (2020). The ERA5 global reanalysis. *Quarterly Journal of the Royal Meteorological Society*, *146*(730), 1999–2049. https://doi.org/10.1002/qj.3803

Heukamp, F. O., Brandt, P., Dengler, M., Tuchen, F. P., McPhaden, M. J., & Moum, J. N. (2022). Tropical instability waves and wind-forced cross-equatorial flow in the central Atlantic Ocean. *Geophysical Research Letters*, *49*, e2022GL099325. https://doi.org/10.1029/2022GL099325

Hisard, P., & Hénin, C. (1987). Response of the equatorial Atlantic Ocean to the 1983-1984 wind from the Programme Français Océan et Climat Dans l'Atlantique equatorial cruise data set. *Journal of Geophysical Research*, *92*(C4), 3759–3768. https://doi.org/10.1029/JC092iC04p03759

Holmes, R. M., & Thomas, L. N. (2016). Modulation of tropical instability waves by equatorial Kelvin waves. *Journal of Physical Oceanography*, *46*(9), 2623–2643. https://doi.org/10.1175/JPO-D-16-0064.1

Hormann, V., & Brandt, P. (2009). Upper equatorial Atlantic variability during 2002 and 2005 associated with equatorial Kelvin waves. *Journal of Geophysical Research*, *114*, C03007. https://doi.org/10.1029/2008JC005101

Hormann, V., Lumpkin, R., & Perez, R. C. (2013). A generalized method for estimating the structure of the equatorial Atlantic cold tongue: Application to drifter observations. *Journal of Atmospheric and Oceanic Technology*, *30*(8), 1884–1895. https://doi.org/10.1175/JTECH-D-12-00173.1

Huang, B., Liu, C., Banzon, V., Freeman, E., Graham, G., Hankins, B., et al. (2021). Improvements of the daily optimum interpolation Sea Surface temperature (DOISST) version 2.1. *Journal of Climate*, *34*(8), 2923–2939. https://doi.org/10.1175/JCLI-D-20-0166.1

Inoue, R., Lien, R.-C., Moum, J. N., Perez, R. C., & Gregg, M. C. (2019). Variations of equatorial shear, stratification, and turbulence within a tropical instability wave cycle. *Journal of Geophysical Research: Oceans*, *124*, 1858–1875. https://doi.org/10.1029/2018JC014480

JPL. (2020). JPL CAP SMAP Sea Surface salinity products (Version 5.0) [Dataset]. PO.DAAC. https://doi.org/10.5067/SMP50-3TMCS

Keenlyside, N. S., & Latif, M. (2007). Understanding equatorial Atlantic interannual variability. *Journal of Climate*, *20*(1), 131–142. https://doi.org/10.1175/JCLI3992.1

Kim, D., Lee, S.-K., Lopez, H., Foltz, G. R., Wen, C., West, R., & Dunion, J. (2023). Increase in Cape Verde hurricanes during Atlantic Niño. *Nature Communications*, *14*(1), 3704. https://doi.org/10.1038/s41467-023-39467-5

Körner, M., Claus, M., Brandt, P., & Tuchen, F. P. (2022). Sources and pathways of intraseasonal meridional kinetic energy in the equatorial Atlantic Ocean. *Journal of Physical Oceanography*, *52*(10), 2445–2462. https://doi.org/10.1175/JPO-D-21-0315.1

Lee, S.-K., Lopez, H., Tuchen, F. P., Kim, D., Foltz, G. R., & Wittenberg, A. T. (2023). On the genesis of the 2021 Atlantic Niño. *Geophysical Research Letters*, *50*, e2023GL104452. https://doi.org/10.1029/2023GL104452

Lee, T., Lagerloef, G., Kao, H.-Y., McPhaden, M. J., Willis, J., & Gierach, M. M. (2014). The influence of salinity on tropical Atlantic instability waves. *Journal of Geophysical Research: Oceans*, *119*, 8375–8493. https://doi.org/10.1002/2014JC010100

Lim, H.-G., Dunne, J. P., Stock, C. A., Ginoux, P., John, J. G., & Krasting, J. (2022). Oceanic and atmospheric drivers of post El-Niño chlorophyll rebound in the equatorial Pacific. *Geophysical Research Letters*, *49*, e2021GL096113. https://doi.org/10.1029/2021GL096113

Losada, T., Rodríguez-Fonseca, B., Janicot, S., Gervois, S., Chauvin, F., & Ruti, P. (2010). A multi-model approach to the Atlantic equatorial mode: Impact on the West African monsoon. *Climate Dynamics*, *35*(1), 29–43. https://doi.org/10.1007/s00382-009-0625-5

Lübbecke, J. F., & McPhaden, M. J. (2013). A comparative stability analysis of Atlantic and Pacific Niño modes. *Journal of Climate*, *26*(8), 5965–5980. https://doi.org/10.1175/JCLI-D-12-00758.1

Lübbecke, J. F., Rodríguez-Fonseca, B., Richter, I., Martín-Rey, M., Losada, T., Polo, I., & Keenlyside, N. S. (2018). Equatorial Atlantic variability—Modes, mechanisms, and global teleconnections. *WIREs Climate Change*, *9*(4), e527. https://doi.org/10.1002/wcc.527

Lumpkin, R., & Garzoli, S. L. (2011). Interannual to decadal changes in the western South Atlantic's surface circulation. *Journal of Geophysical Research*, *116*, C01014. https://doi.org/10.1029/2010JC006285

Martín-Rey, M., Vallès-Casanova, I., & Pelegrí, J. (2023). Upper-ocean circulation and tropical Atlantic interannual modes. *Journal of Climate*, *36*(8), 2625–2643. https://doi.org/10.1175/JCLI-D-22-0184.1

Meissner, T., Wentz, F. J., & Le Vine, D. M. (2018). The salinity retrieval Algorithms for the NASA aquarius version 5 and SMAP version 3 releases. *Remote Sensing*, *10*(7), 1121. https://doi.org/10.3390/rs10071121

Menkes, C. E. R., Kennan, S. C., Flament, P. J., Dandonneau, Y., Masson, S., Biessy, B., et al. (2002). A whirling ecosystem in the equatorial Atlantic. *Geophysical Research Letters*, *29*(11), 1553. https://doi.org/10.1029/2001GL014576

Nobre, C., & Shukla, J. (1996). Variation of sea surface temperature, wind stress, and rainfall over the tropical Atlantic and South America. *Journal of Climate*, *9*(10), 2464–2479. https://doi.org/10.1175/1520-0442(1996)009<2464:VOSSTW>2.0.CO;2

Olivier, L., Reverdin, G., Hasson, A., & Boutin, J. (2020). Tropical instability waves in the Atlantic Ocean: Investigating the relative role of sea surface salinity and temperature from 2010 to 2018. *Journal of Geophysical Research: Oceans*, *125*, e2020JC016641. https://doi.org/10.1029/2020JC016641

Perez, R. C., Foltz, G. R., Lumpkin, R., & Schmid, C. (2019). Direct measurements of upper ocean horizontal velocity and vertical shear in the tropical North Atlantic at 4°N, 23°W. *Journal of Geophysical Research: Oceans*, *124*, 4133–4151. https://doi.org/10.1029/2019JC015064

Perez, R. C., & Kessler, W. S. (2009). Three-dimensional structure of tropical cells in the central equatorial Pacific Ocean. *Journal of Physical Oceanography*, *39*(1), 27–49. https://doi.org/10.1175/2008JPO4029.1

Perez, R. C., Lumpkin, R., Johns, W. E., Foltz, G. R., & Hormann, V. (2012). Interannual variations of Atlantic tropical instability waves. *Journal of Geophysical Research*, *117*, C03011. https://doi.org/10.1029/2011JC007584

Prigent, A., Lübbecke, J., Bayr, T., Latif, M., & Wengel, C. (2020). Weakened SST variability in the tropical Atlantic Ocean since 2000. *Climate Dynamics*, *54*(5–6), 2731–2744. https://doi.org/10.1007/s00382-020-05138-0

Radenac, M.-H., Jouanno, J., Tchamabi, C. C., Awo, F. M., Bourlès, B., Arnault, S., & Aumont, O. (2020). Physical drivers of the nitrate seasonal variability in the Atlantic cold tongue. *Biogeosciences*, *17*(2), 529–545. https://doi.org/10.5194/bg-17-529-2020

Richter, I., Behera, S. K., Doi, T., Taguchi, B., Masumoto, Y., & Xie, S.-P. (2014). What controls equatorial Atlantic winds in boreal spring? *Climate Dynamics*, *43*(11), 3091–3104. https://doi.org/10.1007/s00382-014-2170-0

Richter, I., Behera, S. K., Masumoto, Y., Taguchi, B., Sasaki, H., & Yamagata, T. (2013). Multiple causes of interannual sea surface temperature variability in the equatorial Atlantic Ocean. *Nature Geoscience*, *6*(1), 43–47. https://doi.org/10.1038/ngeo1660

Richter, I., Doi, T., Behera, S. K., & Keenlyside, N. (2017). On the link between mean state biases and prediction skill in the tropics: An atmospheric perspective. *Climate Dynamics*, *50*(9–10), 3355–3374. https://doi.org/10.1007/s00382-017-3809-4

Rodríguez-Fonseca, B., Polo, I., García-Serrano, J., Losada, T., Mohino, E., Mechoso, C. R., & Kucharski, F. (2009). Are Atlantic Niños enhancing Pacific ENSO events in recent decades? *Geophysical Research Letters*, *36*, L20705. https://doi.org/10.1029/2009GL040048

Rugg, A., Foltz, G. R., & Perez, R. C. (2016). Role of mixed layer dynamics in tropical North Atlantic interannual sea surface temperature variability. *Journal of Climate*, *29*(22), 8083–8101. https://doi.org/10.1175/JCLI-D-15-0867.1

Sherman, J., Subramaniam, A., Gorbunov, M. Y., Fernández-Carrera, A., Kiko, R., Brandt, P., & Falkowski, P. G. (2022). The photophysiological response of nitrogen-limited phytoplankton to episodic nitrogen supply associated with tropical instability waves in the equatorial Atlantic. *Frontiers in Marine Science*, *8*, 814663. https://doi.org/10.3389/fmars.2021.814663

Shi, Q., Zhang, R.-H., & Tian, F. (2023). Impact of the deep chlorophyll maximum in the equatorial Pacific as revealed in a coupled ocean GCM-ecosystem model. *Journal of Geophysical Research: Oceans*, *128*, e2022JC018631. https://doi.org/10.1029/2022JC018631

Shi, W., & Wang, S. (2021). Tropical instability wave modulation of chlorophyll-a in the Equatorial Pacific. *Scientific Reports*, *11*(1), 22517. https://doi.org/10.1038/s41598-021-01880-5

Song, Q., Tang, Y., & Aiki, H. (2023). Dual wave energy sources for the Atlantic niño events Identified by wave energy flux in Case studies. *Journal of Geophysical Research: Oceans*, *128*, e2023JC019972. https://doi.org/10.1029/2023JC019972

Specht, M. S., Jungclaus, J., & Bader, J. (2021). Identifying and characterizing subsurface tropical instability waves in the Atlantic Ocean in simulations and observations. *Journal of Geophysical Research: Oceans*, *126*, e2020JC017013. https://doi.org/10.1029/2020JC017013

Tian, F., Zhang, R.-H., & Wang, X. (2019). A positive feedback onto ENSO due to tropical instability wave (TIW)-induced chlorophyll effects in the Pacific. *Geophysical Research Letters*, *46*, 889–897. https://doi.org/10.1029/2018GL081275

Tuchen, F. P., Brandt, P., Claus, M., & Hummels, R. (2018). Deep intraseasonal variability in the central equatorial Atlantic. *Journal of Physical Oceanography*, *48*(12), 2851–2865. https://doi.org/10.1175/JPO-D-18-0059.1

Tuchen, F. P., Brandt, P., Hahn, J., Hummels, R., Krahmann, G., Bourlès, B., et al. (2022). Two decades of full-depth current velocity observations from a moored observatory in the central equatorial Atlantic at 0°N, 23°W. *Frontiers in Marine Science*, *9*, 910979. https://doi.org/10.3389/fmars.2022.910979

Tuchen, F. P., Brandt, P., Hahn, J., Hummels, R., Krahmann, G., Bourlès, B., et al. (2023). Data product of full-depth current velocity observations at 0°N, 23°W from 2001–2023 (v2.0) [Dataset]. Pangaea. https://doi.org/10.1594/PANGAEA.963935

Tuchen, F. P., Perez, R. C., Foltz, G. R., Brandt, P., & Lumpkin, R. (2022). Multidecadal intensification of Atlantic tropical instability waves. *Geophysical Research Letters*, *49*, e2022GL101073. https://doi.org/10.1029/2022GL101073

Vallès-Casanova, I., Lee, S.-K., Foltz, G. R., & Pelegrí, J. L. (2020). On the spatiotemporal diversity of Atlantic Niño and associated rainfall variability over West Africa and South America. *Geophysical Research Letters*, *47*, e2020GL087108. https://doi.org/10.1029/2020GL087108

von Schuckmann, K., Brandt, P., & Eden, C. (2008). Generation of tropical instability waves in the Atlantic Ocean. *Journal of Geophysical Research*, *113*, C08034. https://doi.org/10.1029/2007JC004712

Wu, Q., & Bowman, K. P. (2007). Interannual variations of tropical instability waves observed by the Tropical Rainfall Measuring Mission. *Geophysical Research Letters*, *34*, L09701. https://doi.org/10.1029/2007GL029719

Xue, A., Jin, F.-F., Zhang, W., Boucharel, J., & Kug, J.-S. (2023). Parameterizing the nonlinear feedback on ENSO from tropical instability waves (TIWs) by nonlinear eddy thermal diffusivity. *Climate Dynamics*, *61*(7–8), 3525–3540. https://doi.org/10.1007/s00382-023-06744-4

Yang, Y., Wu, L., Cai, W., Jia, F., Ng, B., Wang, G., & Geng, T. (2022). Suppressed Atlantic Niño/Niña variability under greenhouse warming. *Nature Climate Change*, *12*(9), 814–821. https://doi.org/10.1038/s41558-022-01444-z

Yu, Z., McCreary, J. P., Jr., & Proehl, J. A. (1995). Meridional asymmetry and energetics of tropical instability waves. *Journal of Physical Oceanography*, *25*(12), 2997–3007. https://doi.org/10.1175/1520-0485(1995)025<2997:MAAEOT>2.0.CO;2

Zebiak, S. E. (1993). Air–Sea interaction in the equatorial Atlantic region. *Journal of Climate*, *6*(8), 1567–1586. https://doi.org/10.1175/1520-0442(1993)006<1567:AIITEA>2.0.CO;2